



Ternary heterojunction in rGO-coated Ag/Cu₂O catalysts for boosting selective photocatalytic CO₂ reduction into CH₄

Zhiling Tang^a, Wenjie He^a, Yingli Wang^a, Yuechang Wei^{a,b,*}, Xiaolin Yu^c, Jing Xiong^{a,b}, Xiong Wang^a, Xiao Zhang^a, Zhen Zhao^a, Jian Liu^a

^a State Key Laboratory of Heavy Oil Processing, China University of Petroleum, Beijing 102249, China

^b Key Laboratory of Optical Detection Technology for Oil and Gas, China University of Petroleum, Beijing 102249, China

^c State Key Laboratory for Structural Chemistry of Unstable and Stable Species, Beijing National Laboratory for Molecular Sciences (BNLMS), CAS Research/Education Center for Excellence in Molecular Sciences, Institute of Chemistry, Chinese Academy of Sciences, Beijing 100190, China

ARTICLE INFO

Keywords:

Photocatalysts
CO₂ photoreduction
Reduced graphene oxide
Cu₂O octahedral nanocrystal
Ternary heterojunction

ABSTRACT

Herein, the ternary catalyst of reduced graphene oxide (rGO)-coated Ag/Cu₂O-octahedron nanocrystals (Ag/Cu₂O@rGO) was successfully fabricated by method of water bath combining with gas-bubbling-assisted membrane reduction. Supported Ag nanoparticles with low fermi energy can enrich the photogenerated electrons originated from visible light-driven Cu₂O octahedral nanocrystals. The surface extended π bond of coated rGO nanolayers on Ag/Cu₂O can further capture photoelectrons and improve adsorption-activation capacities for reactants. Ag_n/Cu₂O@rGO catalysts with ternary rGO-Ag-Cu₂O heterojunction exhibit excellent performance during selective photocatalytic CO₂ reduction with H₂O into CH₄. Ag₄/Cu₂O@rGO catalyst has the highest formation rate (82.6 $\mu\text{mol g}^{-1} \text{h}^{-1}$) and selectivity (95.4%) of CH₄ product. Combined with the results of in-situ DRIFT spectra and density functional theory calculations, the photocatalytic mechanism is proposed: the protonation of CO* intermediate is key step for selective photocatalytic CO₂ reduction into CH₄. It provides one novel strategy to development of high-efficient photocatalyst for selective CO₂ conversion into C1 chemicals.

1. Introduction

Artificial photosynthesis (photocatalytic conversion), as a promising technology for converting carbon dioxide (CO₂) with water (H₂O) into valuable chemicals with solar, is considered to be one of the effective ways to achieve carbon neutrality [1,2]. The reduction process of CO₂ involves multiple consecutive proton-coupled electron transfer steps to produce all kinds of reduction products (CO, CH₄ and CH₃OH, etc). It is still a huge challenge to convert the extremely stable CO₂ molecules with the dissociation energy of C=O bond (750 kJ mol⁻¹) to other energy substances by photoreduction, and the photocatalyst is crucial to achieve the CO₂ conversion. For the past few years, a great deal of high-efficient photocatalysts have been reported for light-driven CO₂ conversion, such as ZnS [3], TiO₂ [4–6], ZnO [7], Bi₂MoO₆ [8,9] and so on, but their insufficient photocatalytic performances with high energy loss is difficult to meet the practical application and commercialization [10,11]. Thus, it is still an urgent need to the construction of high-efficient photocatalysts and the in-depth understanding the photocatalytic mechanism during CO₂ conversion.

The reaction essence of light-driven catalytic CO₂ conversion with H₂O is the heterogenous catalysis occurring in the gas-solid interface, and the catalytic performance of the materials is strongly related to the absorption efficiency of sunlight, the separation efficiency of photo-generated carries, and the adsorption-activation property for CO₂ and H₂O, which depends on the surface microstructure and composition of the photocatalysts [12–14]. For enhancing absorption efficiency of sunlight, it is particularly critical to develop semiconductors with a narrow band gap and sensitive to visible light, which is mainly proportion of solar energy. Among the reported semiconductor photocatalysts, cuprous oxide (Cu₂O) is a potential p-type semiconductor with wide visible-light response range and high photoelectric conversion efficiency [15], and it displays attractive prospects in solar energy conversion and heterogeneous photocatalysis. Nowadays, the scientists have in-depth investigated the role of crystal phase structures and surface crystal facets during photocatalytic reduction reaction, and it is found that Cu₂O nanocrystals with exposed (111) crystal facet exhibited better catalytic performance during CO₂ photoconversion reaction in comparison with their exposed (110) and (100) facets [16]. And the

* Corresponding author at: State Key Laboratory of Heavy Oil Processing, China University of Petroleum, Beijing 102249, China.

E-mail address: weiy@cup.edu.cn (Y. Wei).

<https://doi.org/10.1016/j.apcatb.2022.121371>

Received 7 December 2021; Received in revised form 21 March 2022; Accepted 2 April 2022

Available online 6 April 2022

0926-3373/© 2022 Elsevier B.V. All rights reserved.

unsaturated Cu ions located at the exposed (111) facet of Cu₂O nanocrystals as active sites can promote the enhancing separation efficiency of photogenerated carriers during photocatalysis reaction. However, bare Cu₂O has the low reactant adsorption capacity and the limited photo-generated electrons enrichment property, which leads to the insufficient efficiency for photocatalytic CO₂ conversion. Thus, the introduction of the other active components on the surface of Cu₂O nanocrystals is necessary to enhance their photocatalytic performance during CO₂ reduction with H₂O.

The graphene materials with abundant surface extended π bond are considered to be one of the promising chemical components for adsorption and activation for reactants (CO₂ and H₂O), and it is also beneficial to maintain the stability of Cu₂O nanocrystals [17]. Graphene oxide (GO) is a star material favored in the field of photocatalysis by virtue of its ultra-fast optical response, strong adsorption capacity and excellent charge carrier mobility. It has been found that the reduced GO (rGO) material can provide the abundant active sites for improving adsorption-activation capacity for H₂O and CO₂ because of its surface unique functional groups [8,18–20]. It is well known that the activity of the photocatalysts is closely associated with the number of available catalytic sites, thus, the rGO-based material with large specific surface area is potential to improve photocatalytic efficiency during light-driven CO₂ conversion.

Compared with the photocatalytic CO₂ reduction into CO product, CH₄ product can store more chemical energy originated from solar energy. But it is still an urgent challenge for enhancing the product selectivity during photocatalytic CO₂ conversion with H₂O into CH₄. Considering that the enrichment of photogenerated charges is essential to enhance the product selectivity of CH₄, the construction of multi-variate heterojunctions is considered to be a promising strategy to enhance the utilization efficiency of photogenerated electrons [21,22]. Recently, they have been found that the combining metal oxides with plasmonic metal nanostructures (Au, Ag, etc.) can further affect the reaction intermediates and pathways [10,23,24]. Au and Ag nanoparticles (NPs) with special surface plasmon resonance (SPR) effect can act as energy donors, and realize the transfer of solar energy to metal oxides in the process of resonance energy transfer, which broadens the wavelength range and improves the separation efficiency of photogenerated carriers. Taking the above characteristics into account, the construction of multicomponent catalysts, combining the CO₂-adsorption site (graphene-based materials) with the path-change site (plasmonic metal nanostructures), might be crucial to enhance the selectivity of CH₄ product during photocatalytic CO₂ conversion with H₂O. However, it is still rarely systematic studies concerning the ternary metal-oxide-rGO heterojunction for improving photocatalytic performance of CO₂ reduction. Thus, the innovative design and fabrication of ternary heterojunction catalysts is potential to promote the improving catalytic activity for selective CO₂ photoreduction into CH₄.

Herein, the ternary catalysts of reduced graphene oxide (rGO)-coated Ag/Cu₂O-octahedron nanocrystals (Ag/Cu₂O@rGO) were devised and fabricated by the three-step method. Ag NPs with uniform sizes are supported on the surface of regular Cu₂O octahedral nanocrystals with exposed 100% (111) facet by the method of the improved gas-bubbling-assisted membrane reduction (GBMR) [25]. The secondary reduction strategy was employed for the construction of novel ternary rGO-Ag-Cu₂O heterojunction. Supported Ag NPs can enrich the photoelectrons originated from visible light-driven Cu₂O octahedral nanocrystals, and the coated rGO nanolayers on the surface of Ag/Cu₂O can enhance the adsorption-activation capacities for the reactants. Ag/Cu₂O@rGO catalyst with the ternary rGO-Ag-Cu₂O heterojunction exhibits excellent catalytic performance during selective CO₂ photoreduction with H₂O into CH₄. Based on the results of photoelectrochemical characterizations, in-situ diffuse reflectance infrared Fourier transform (DRIFT) spectra and density functional theory (DFT) calculations, the role of ternary rGO-Ag-Cu₂O heterojunction in the protonation of CO* intermediate is proposed and in-depth discussed. The work provided an

innovation ternary heterojunction strategy for reducing the Gibbs free energy of CHO* formation during selective photocatalytic CO₂ reduction into CH₄.

2. Experimental sections

2.1. Syntheses of the photocatalysts

The ternary Ag/Cu₂O@rGO photocatalysts of rGO-coated Ag/Cu₂O-octahedron nanocrystals were successfully synthesized by three-step method: i) Synthesis of octahedral Cu₂O nanocrystals with exposed (111) facet by one-pot water bath method [26]; ii) Fabrication of uniform Ag NPs supported on the surface of Cu₂O octahedral nanocrystals by GBMR method; iii) Construction of rGO nanolayers-coated Ag/Cu₂O catalyst by the self-assembly method. The syntheses schematic of the Ag/Cu₂O@rGO catalysts is shown in Fig. 1. Firstly, the shape control of Cu₂O (111) crystal facet was achieved by preferential adsorption of PVP during the crystal growth process. Unsaturated Cu on (111) facet of Cu₂O interacts actively with PVP. With the introduction of PVP, it is stably adsorbed on the (111) facet, limiting the growth rate of the (001) and (110) facets. The molar ratio of PVP to CuCl₂·2H₂O increases to 30, resulting in the exposure of the (111) facet and formation of an octahedral structure. The orange-red octahedral Cu₂O (Fig. 3A) nanocrystals were obtained. Secondly, the particle size of Ag NPs in the synthesized Ag/Cu₂O catalyst was controlled by GBMR method. As a reducing agent, NaBH₄ was uniformly dispersed in the solution, so that Ag⁺ ions adsorbed on the Cu₂O surface were reduced slowly, avoiding the agglomeration of Ag NPs caused by the concentration gradient of the NaBH₄ solution. On the other hand, the addition of PVP as a stabilizer could control the growth process of Ag nuclei and adjust the particle size of Ag NPs. After introduction of Ag NPs supported on the surface of Cu₂O nanocrystals, the color of product solution changed from orange red to dark red, and the morphology of Ag/Cu₂O catalyst is shown in Fig. 3B. Thirdly, the rGO nanolayers-coated Ag/Cu₂O (Ag/Cu₂O@rGO) catalyst by the self-assembly method. The ultra-thin GO with good electron transport mobility, purchased from Nanjing Zeyou Environmental Protection Technology Co. LTD, has abundant oxygen-containing functional groups. With the addition of the exfoliated GO solution, the prepared Ag/Cu₂O can be strongly adsorbed on the GO surface because of the condensation reaction of functional groups. Subsequently, Ag/Cu₂O@GO materials would be reduced to Ag/Cu₂O@rGO photocatalysts by NaBH₄ solution. Finally, the Ag/Cu₂O@rGO catalysts were obtained after the processes of the centrifugation, washing and vacuum drying at 60 °C for 6 h. The obtained products are denoted as Ag_n-Cu₂O@rGO, where n is the actual weight percent of Ag to Cu₂O@rGO (2, 4 and 6 wt%) determined by the inductively coupled plasma-atomic emission spectrometry. The synthesis processes of Ag_n-Cu₂O@rGO catalysts are listed in Supporting Information in detail.

2.2. Characterizations of the photocatalysts

The analyses of surface microstructures and chemical compositions of the catalysts were carried out on a FEI Quanta 200 F scanning electron microscopy (SEM) and JEOL JEM 2100 transmission electron microscopy (TEM). The phase structure of the photocatalysts was performed on a powder X-ray diffractometer (XRD, Shi-madzu XRD 6000). The chemical bonds or functional information were obtained by using the Fourier transform infrared spectroscopy (FT-IR) method. To study on the absorption property of the ultraviolet and visible range, UV-visible spectra were carried out on a Shimadzu UV-2600 UV-vis spectrophotometer in the range of 200–800 nm. The Brunauer-Emmett-Teller (BET) method was carried out to calculate the specific surface area of the samples. In-situ DRIFT spectra were measured on a FT-IR spectrometer (Thermo Scientific Nicolet iS50) with an in-situ diffuse reflectance cell (Harrick). Under the condition of the mixture of CO₂ and H₂O, the samples in the in-situ reactor were heated from room temperature to

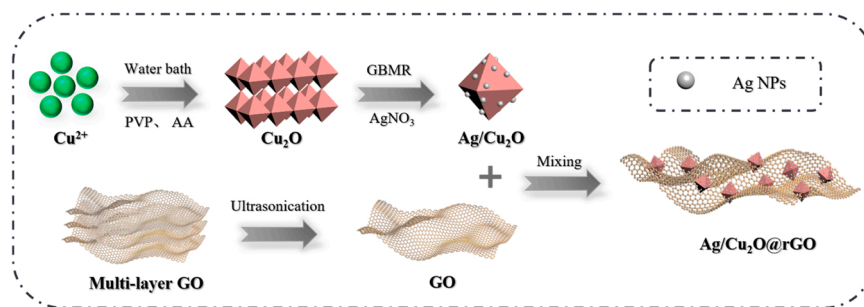


Fig. 1. Schematic of synthesis procedures for Ag/Cu₂O@rGO photocatalyst.

200 °C, and N₂ purging was used to remove surface adsorbates. After cooling to room temperature, the infrared spectrum in the dark was collected as background data. Then, the data were collected in the dark and light at the flow rate (50 mL min⁻¹) of CO₂. The isotopic tracing test was carried out on 5977B GC/MS (Agilent) by using ¹³CO₂ and D₂O as reactants under the same as test condition of photocatalytic CO₂ reduction. Fluorescence luminescence (PL) spectroscopy were tested using the F-4500 fluorescence luminescence spectrometer (Hitachi, Japan). The excitation source was monochromatic light with a wavelength of 380 nm, and the receiving fluorescence range was from 400 nm to 700 nm. X-ray photoelectron spectroscopy (XPS) with Auger electron spectroscopy (AES) and valence band-XPS (VB-XPS) measurements were obtained on the PerkinElmer PHI-1600 ESCA spectrometer equipped with the multi-channel detector. The spectra were excited by using the Mg K α X-ray source ($h\nu = 1253.6$ eV, $1\text{ eV} = 1.603 \times 10^{-19}$ J). The binding energy of all elements in the photocatalysts was calibrated by the binding energy of C 1 s at 284.8 eV. All density functional theory (DFT) calculations were carried out in the framework of the Vienna ab initio Simulation Package (VASP). All the structures and energy were allowed to relax below 0.05 eV Å⁻¹. The calculations of charge density difference were employed to analyze the movement and distribution of the charge. The adsorption energy E_{ads} was calculated by a standard formula: $E_{\text{ads}} = E_{\text{catalyst} + \text{CO}} - E_{\text{catalyst}} - E_{\text{CO}}$.

Photoelectrochemical (PEC) measurements were performed by the three-electrode system on an electrochemical workstation (CHI660E). Typically, the Pt net was employed as the counter electrode, the Ag/AgCl electrode is the reference electrode, and the determinand is the working electrodes. For the preparation of the working electrode, the catalyst (25 mg) was dispersed in deionized water (384 μ L) and ethanol (96 μ L). After sonicating for 20 min, Nafion (10 μ L) was added into the mixture and sonicated for 5 min. The mixture (5 μ L) was deposited on the surface of the glassy carbon electrode (the area was 1 cm²) and dried naturally to form one thin film at room temperature. The Na₂SO₄ solution (0.1 mol L⁻¹) was acted as electrolyte. The test environment of transient photocurrent in this system was to switch the lights on and off every 50 s, and the catalysts were excited by the Xe lamp (300 W). Mott-Schottky experiments was performed with two different frequencies (500 and 1000 Hz), and the test frequency of electrochemical impedance spectra (EIS) ranges from 0.1 to 100,000 Hz.

2.3. Tests on photocatalytic CO₂ reduction with H₂O

The tests on the photocatalytic CO₂ reduction were performed in a sealed system. The Labsolar II device designed and manufactured by Perfectlight Company was chosen as the activity test device for this experiment (vacuum degree is -0.1 MPa), and the GC-9560 produced by HuaAiSePu Company was chosen as the online gas phase component detection device. The effective volume of the reactor is 250 mL. In order to simulate the photosynthesis of natural plants, one xenon lamp (300 W) was chosen as the light source, and added a 380 nm external filter to make the light source only retain the visible light. The photocatalysts (0.15 g) were evenly coated on a piece of watch glass (diameter

is ~ 6.0 cm) with the deionized water (2.0 mL), and the area of receiving light is ~ 28.3 cm². The mixed sample was uniformly ultrasound and put into the photoreaction system. Before introduction of light irradiation, the photoreaction system was thoroughly vacuum-treated (3 times), and then CO₂ was injected into the internal circulation reactor until the pressure reached 80.0 kPa. The intensity of the incident light measured with a spectroradiometer is ~ 80 mW/cm². After starting the light source and the gas chromatograph automatic sampling device, the sample was analyzed each hour, and the reaction test was carried out for 8 h.

The photon efficiency is an important standard to measure the efficiency of the photocatalytic reaction to convert light energy. The number of photons can be effectively measured and calculated by using a single-wavelength light source (380 nm). The number of photons converted by the reaction is converted by the molar amount of the product produced and the corresponding number of photons required. The ratio of the two is the efficiency of tourism, and the specific formula is as follows:

$$\text{AQE}[\%] = \frac{\text{Number of } \text{CH}_4 \times 8 + \text{Number of } \text{CO} \times 2}{\text{Number of Incident Photos}} \times 100\% \quad (1)$$

3. Results and Discussions

3.1. Microstructures of Ag/Cu₂O@rGO photocatalysts

The phase structure of Cu₂O, Cu₂O@rGO, Ag/Cu₂O and Ag_n/Cu₂O@rGO catalysts is investigated by the XRD spectra and FT-IR spectra, and the results are exhibited in Fig. 2. As displayed in Fig. 2A, the octahedral Cu₂O nanocrystals exhibit the six different peaks located at 29.6, 36.4, 42.3, 61.3, 73.5 and 77.3°, which is assigned to the characteristic diffraction peaks of the (110), (111), (200), (220), (311) and (222) facets of cubic-phased Cu₂O (JCPDS No. 05-0667), respectively. After introduction of supported Ag NPs, Ag/Cu₂O and Ag/Cu₂O@rGO catalysts show the two weak diffraction peaks located at 38.1 and 44.3°, which is assigned to the (111) and (200) facets of cubic-phased Ag NP (JCPDS No. 04-0783), suggesting that Ag NPs are deposited on the surface of octahedral Cu₂O nanocrystals. After further introduction of coated rGO nanolayer, the characteristic diffraction peaks of Cu₂O@rGO catalyst are the same as those of Cu₂O nanocrystals, and the diffraction peak assigned to rGO nanolayers is not found. It suggests that the thickness of rGO coating exceeds the detection limit of XRD technology, in other words, the coated rGO layers have the nano-scale thickness. It is well known that the ultrathin rGO nanolayers have good light transmittance, thus, the coated rGO nanolayers will not interference with absorption and activation efficiency of Ag/Cu₂O nanocrystals for visible light.

FT-IR spectra was further used to investigate the microstructure of rGO-coated nanolayers in the Ag/Cu₂O@rGO catalysts with ternary heterojunction. As shown in Fig. 2B, rGO nanolayers exhibit four FT-IR absorption peaks located at 1043, 1394, 1622 and 3450 cm⁻¹. The absorption peak centered at 1622 cm⁻¹ is assigned to the characteristic peak of C=C bond in the entire graphene skeleton, and the others

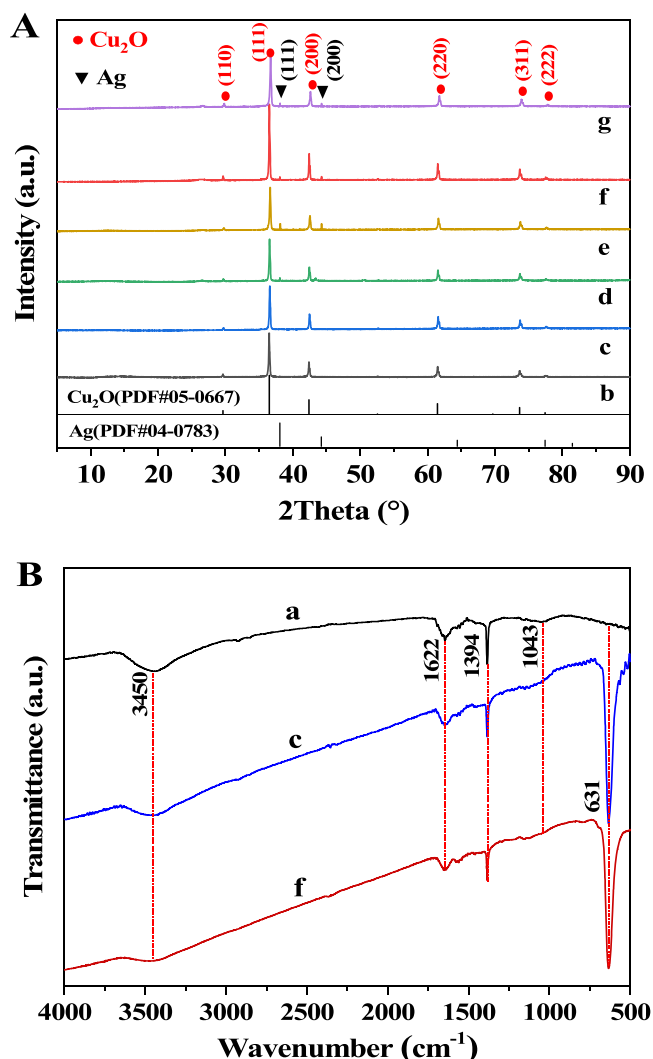


Fig. 2. XRD patterns (A) and FT-IR spectra (B) of rGO, Cu₂O, Cu₂O@rGO, Ag/Cu₂O and Ag_n/Cu₂O@rGO catalysts. (a) rGO; (b) Cu₂O; (c) Cu₂O@rGO; (d) Ag/Cu₂O; (e) Ag₂/Cu₂O@rGO; (f) Ag₄/Cu₂O@rGO; (g) Ag₆/Cu₂O@rGO.

absorption bands at 3450, 1394 and 1043 cm⁻¹ are ascribed to the stretching and bending vibration of O-H bond and the stretching vibration of C-O bond, respectively [27]. For Cu₂O@rGO and Ag₄/Cu₂O@rGO catalysts, one new absorption peak located at 631 cm⁻¹ is found, which is designated to the stretching vibration of the Cu-O bond [28], and the intensity of the absorption peaks corresponding to the oxygen-containing functional groups weakens obviously and even disappears (at 1043 cm⁻¹), suggesting that there is the strong interaction between rGO and Ag/Cu₂O nanocrystals at the interface of ternary rGO-Ag-Cu₂O heterojunction, which may be in favor of the transfer and enrichment of photoinduced electrons. In addition, Table S1 shows the structural physical parameters of Cu₂O, Ag/Cu₂O, Cu₂O@rGO and Ag_n/Cu₂O@rGO catalysts including surface areas, pore volumes and Ag actual contents. After introduction of supported Ag NPs and coated rGO nanolayers, the surface areas and pore volumes of the catalysts have not changed obviously, and the nitrogen adsorption-desorption isotherms of the catalysts are shown in Fig. S1.

The morphology and microstructure of Cu₂O and Ag_n/Cu₂O@rGO catalysts are further observed by SEM, TEM and STEM images. From the SEM image shown in Fig. 3A, Cu₂O nanocrystals show the regular octahedron morphology obtained by an appropriate amount of PVP as capping agent, indicating that Cu₂O nanocrystals have eight equivalent crystal facets. Its average edge length of Cu₂O nanocrystals is 300 nm by

statistical analysis of more than 100 nanocrystals. After the introduction of supported Ag NPs, Ag₄/Cu₂O catalyst in Fig. 3B presents the uniformly octahedral structure, and the color of the catalyst changes from orange red to dark red shown in the insets of Figs. 3A and 3B. The supported Ag NPs with uniform sizes have not destroyed the morphology of Cu₂O octahedral nanocrystals in the processes of GBMR method. Although Ag NPs supported on Cu₂O nanocrystals have not been clearly observed in SEM images, the presence of Ag element on the surface of Cu₂O octahedral nanocrystals is verified by the result of SEM-EDS profile exhibited in Fig. S2. As exhibited in Fig. 3C, the coating of rGO nanolayers can be clearly observed together with the uniform Cu₂O octahedral nanocrystals. From optical photograph in inset of Fig. 3C, with introduction of rGO nanolayers and Ag NPs, the color of the catalyst further changes from the dark red to the brown. As shown in Fig. 3D, the square Cu₂O nanoparticles with length of 300 nm can be observed, which is the vertical projection of Cu₂O octahedral nanocrystals. And the ultra-thin rGO nanolayers contacted with Cu₂O nanocrystals are observed. From HRTEM and STEM images of Ag₄/Cu₂O@rGO catalyst exhibited in Fig. 3(E-G), a large number of uniformly distributed Ag NPs with average particle size of 10.7 nm (Fig. S3) are deposited on the surface of Cu₂O nanocrystals. As shown in Fig. 3E, the rGO nanolayers coated on the Ag/Cu₂O nanocrystals exhibit the morphology of ultra-thin nanosheet, and Ag NP as an intermediate medium is between Cu₂O and rGO nanolayers, indicating the formation of ternary rGO-Ag-Cu₂O heterojunction, which is beneficial to enhancing the adsorption efficiency of visible light. Fig. 3F further exhibits the magnified area of ternary rGO-Ag-Cu₂O heterojunction in Fig. 3E. It is noted that the catalyst shows the clearly lattice fringe, and the thickness of rGO nanolayers coated on Ag NP is 1.0 nm. As shown in Fig. 3F, the fringe spacing of 0.25 nm is ascribed to (111) facet of Cu₂O nanoparticles, indicating that the exposed crystal facet of Cu₂O nanocrystals is 100% (111) crystal facet. The fringe spacing (0.24 nm) of one spherical Ag NP clearly corresponds to the exposed (111) crystal plane. As shown in Fig. 3G, it is found that supported Ag NPs on the surface of Cu₂O nanocrystals is further decorated by the rGO nanolayers. The STEM image of the catalysts in Fig. 3H displays the strong interfacial contact between Ag NPs and Cu₂O nanocrystal, which is conducive to the transmission of photogenerated carriers. The elemental mapping images in Fig. 3I reveal the position distribution of each element (C, Cu, O and Ag) in the Ag/Cu₂O@rGO catalyst, which is highly in accordance with the results of TEM images. It indicates the formation of ternary rGO-Ag-Cu₂O heterojunction.

The XPS and AES spectra of the Cu₂O, Ag/Cu₂O and Ag/Cu₂O@rGO catalysts were carried out to further investigate the valence states of surface Cu and Ag elements, and the spectra are exhibited in Fig. 4. As displayed in Fig. 4A, the Cu 2p spectra of Cu₂O nanocrystals show two main XPS peaks located at 932.0 and 951.9 eV, which is assigned to the binding energies of Cu 2p_{3/2} and 2p_{5/2} of surface Cu⁺ species, respectively [29]. And the XPS peak corresponding to Cu²⁺ species (933.6 eV) is not observed. After introduction of supported Ag NPs and coated rGO nanolayers, XPS peaks of Cu 2p have slightly shift to high binding energy, suggesting that the ternary rGO-Ag-Cu₂O heterojunction have the strong electronic-level interaction, which is in favor of the transfer of photoinduced carriers. Fig. 4B exhibits the Ag 3d XPS spectra of Ag/Cu₂O and Ag/Cu₂O@rGO catalysts. The two main peaks located at 368.4 and 374.4 eV are assigned to the binding energies of Ag 3d_{5/2} and Ag 3d_{3/2}, respectively. The spin separation energy (6.0 eV) proves that Ag element is both the metallic and ionic state in Ag/Cu₂O and Ag₄/Cu₂O@rGO catalysts. The deconvolutions of the curves were carried out by the standard rule. The XPS peaks centered at 369.5 and 375.3 eV, 368.4 and 374.4 eV, 367.6 and 373.7 eV are assigned to the Ag 3d 5/2 and 3/2 binding energies of Ag⁰, Ag⁺ and Ag²⁺ species, respectively [30]. It confirms that the metallic (Ag⁰) and ionic (Ag⁺, Ag²⁺) species coexist in Ag/Cu₂O@rGO catalyst. As displayed in Table S2, after introduction of rGO nanolayers, the ratio value of (Ag⁺ and Ag²⁺)/Ag⁰ decreases from 8.09 to 7.55, further suggesting that

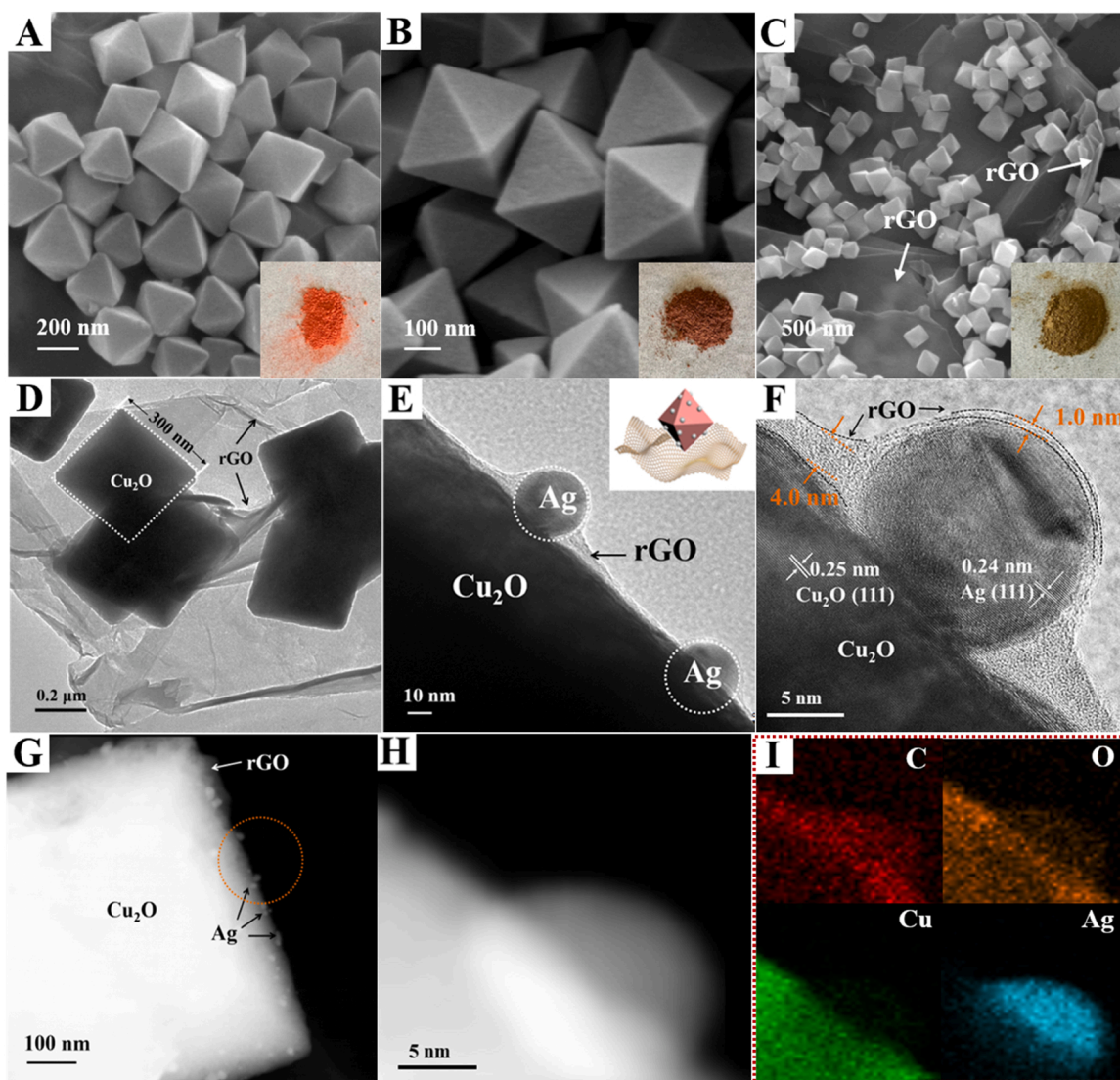


Fig. 3. SEM (A-C), TEM (D-F) and STEM-EDS elemental mapping (G-I) images of Cu₂O (A), Ag₄/Cu₂O (B) and Ag₄/Cu₂O@rGO (C-I) catalysts. The insets in (A-C) images are the digital photographs of Cu₂O, Ag₄/Cu₂O and Ag₄/Cu₂O@rGO catalysts. The inset in (E) is the model image of Ag₄/Cu₂O@rGO catalyst and the (I) images are STEM-EDS elemental mapping (Carbon, red; Oxygen, orange; Cuprum, green; Silver, blue). (For interpretation of the references to colour in this figure, the reader is referred to the web version of this article.)

there is the strong electronic-level interaction between Ag NPs and rGO nanolayers, and rGO nanolayers as an electron donor bond with the circumambient Ag NPs. In consideration of the strong metal (Ag)-support (rGO and Cu₂O) interaction, it is potential to realize vectorial transfer of photogenerated electron-hole pairs in the ternary system with Ag NPs as conducting medium. In addition, the location of the Auger peak depends on the specific chemical state of the substance, which is related to the dielectric and electronic properties of the surrounding environment of the light-excited electrons. Thus, the valence state of Cu element on the surface of the catalysts can be further investigated by the AES spectra, and the results are exhibited in Fig. 4(C-D). It is noted that the Cu LMM AES spectra of Cu₂O and Ag/Cu₂O@rGO catalysts have only one strong peak of kinetic energy located at 916.6 eV, which is belonged to the Cu⁺ species or Cu₂O-type oxide in the catalysts [31]. After introduction of coated rGO nanolayers, the weak peak of kinetic energy at 913.0 eV is observed, which is assigned to the presence of hole in the ligand L bonding of the Cu ion. Combined with the results of XPS and Cu LMM AES spectra, it is worth noted that the Cu⁺ species or Cu₂O-type oxide are main the existing form of surface Cu element in Ag/Cu₂O@rGO catalysts, and the ternary rGO-Ag-Cu₂O heterojunction

have electronic-level interaction.

3.2. The performances for photocatalytic CO₂ reduction with H₂O

The performance measurement for visible light-driven photocatalytic CO₂ reduction into hydrocarbon products was carried out under simulated solar irradiation (≥ 380 nm), and the detailed results are exhibited in Fig. 5 and Table 1. During the reaction processes of photocatalytic CO₂ reduction with H₂O, the two main carbon-containing products are CH₄ and CO accompanied by O₂ product. Fig. 5A shows the evolution of CH₄ product over Cu₂O, Cu₂O@rGO, Ag/Cu₂O and Ag_n/Cu₂O@rGO catalysts. For bare Cu₂O catalyst, the formation rate of CH₄ product is only 4.7 $\mu\text{mol g}^{-1} \text{h}^{-1}$ in Table 1, while it increases to 7.9 $\mu\text{mol g}^{-1} \text{h}^{-1}$ after introduction of coated rGO nanolayers on the Cu₂O nanocrystals. It is attributed to that the rGO nanolayers with extremely narrow band gap can promote the rapid electron distribution and effectively inhibits the recombination of electron-hole pairs originated from photoexcited Cu₂O nanocrystals. Compared with bare Cu₂O catalyst, the formation rate of CH₄ product of Ag/Cu₂O photocatalyst rises to 12.7 $\mu\text{mol g}^{-1} \text{h}^{-1}$, which is attributed to the plasmon resonance effect

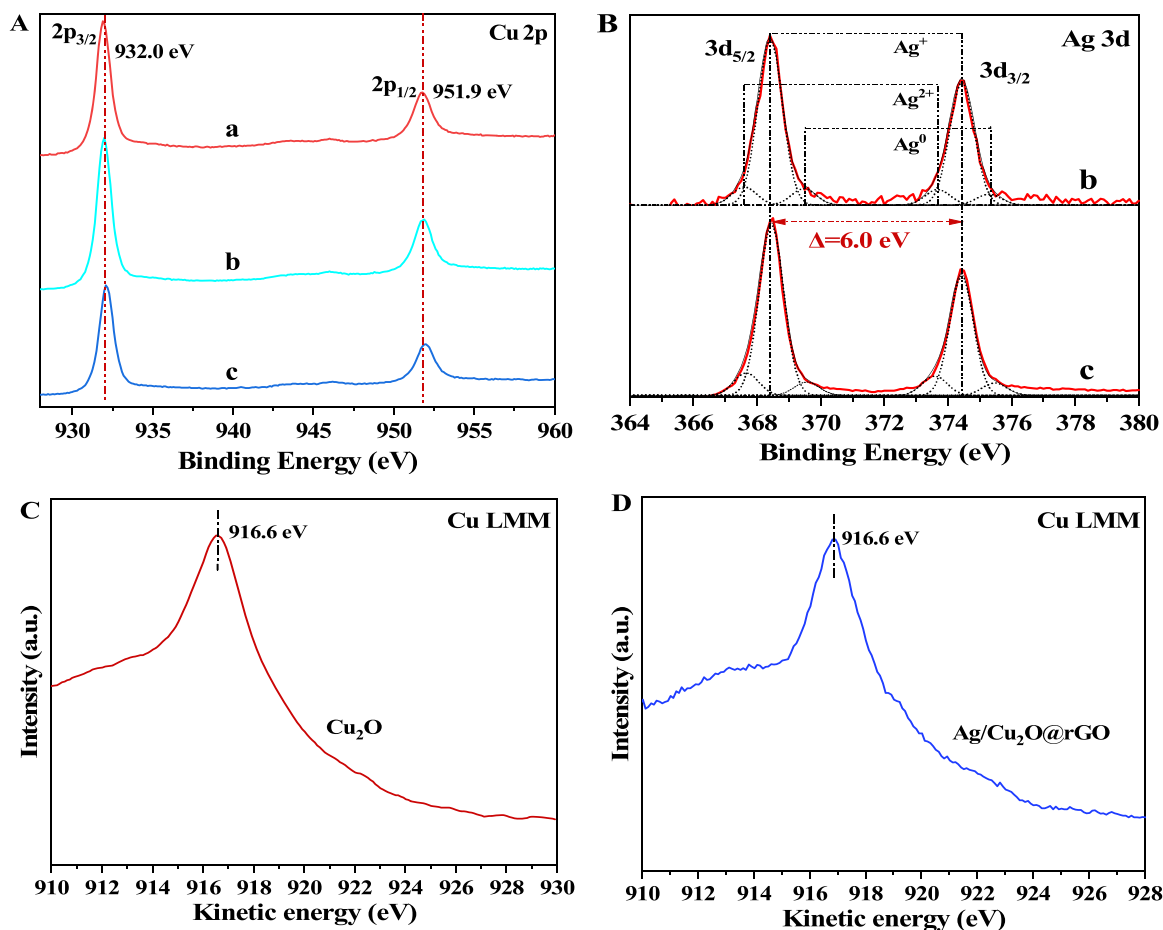


Fig. 4. XPS spectra of Cu 2p (A), Ag 3d (B) and Cu LMM AES (C-D) spectra over Cu₂O, Ag/Cu₂O and Ag₄/Cu₂O@rGO catalysts. (a) Cu₂O; (b) Ag/Cu₂O; (c) Ag₄/Cu₂O@rGO.

of Ag NPs for boosting photocatalytic CO₂ reduction. The supported Ag NPs act as a co-catalyst can capture photoelectrons and constructs the Schottky barrier at the Ag-Cu₂O interface, which effectively prevents the recombination of photoinduced carriers [32]. After introduction of coated rGO nanolayers, the ternary rGO-Ag-Cu₂O heterojunction in the Ag_n/Cu₂O@rGO catalysts can boost the enhancing performance for photocatalytic CO₂ reduction to CH₄. Among the prepared photocatalysts, the Ag₄/Cu₂O@rGO catalyst displays the highest activity for photocatalytic CO₂ conversion, i.e., its formation rate of CH₄ product is 82.6 μmol g⁻¹ h⁻¹, which is 17.6-fold of bare Cu₂O catalyst. It suggests that the synergistic effect of ternary rGO-Ag-Cu₂O heterojunction improves the selectivity of photocatalytic CO₂ reduction into CH₄, which is strongly dependent on the separation efficiency of photoinduced carriers and the enrichment degree of electrons and hydrogen protons [33]. It is also verified that, with increasing of supported Ag loading, the formation rate of CH₄ product over Ag_n/Cu₂O@rGO photocatalyst decreases to 54.1 μmol g⁻¹ h⁻¹, which is ascribed to decrease the surface density of photoinduced electrons over overmuch Ag NPs.

The evolution of CO product over Cu₂O, Cu₂O@rGO, Ag/Cu₂O and Ag_n/Cu₂O@rGO catalysts is shown in Fig. 5B. It is well known that the reaction pathway of photocatalytic CO₂ reduction into CO needs to the participation of two electrons and two hydrogen protons, while it needs to eight electrons and eight hydrogen protons for CH₄ formation. Thus, supported Ag NPs as the enrichment sites of photogenerated electrons prefer to the formation of CH₄ rather than CO product during photocatalytic CO₂ reduction. It is worth noting that Ag/Cu₂O photocatalyst has the lowest formation rate of CO (1.3 μmol g⁻¹ h⁻¹), while the formation rate of CO product over Cu₂O@rGO catalyst is the largest (8.7 μmol g⁻¹ h⁻¹). It suggests that the coated rGO nanolayers can improve

adsorption and activation property for CO₂. It is well known that the reaction of photocatalytic H₂O reduction to H₂ is compete with the photocatalytic CO₂ reduction to CH₄, so the formation rate of H₂ product is also important index to photocatalytic performance, and the result is shown in Fig. S4 and Table 1. Ag/Cu₂O catalyst has the largest formation rate of H₂ product (56.8 μmol g⁻¹ h⁻¹), which is 10-fold of Cu₂O catalyst (5.6 μmol g⁻¹ h⁻¹). It indicates that the supported Ag NPs with low Fermi level can capture the photoinduced electrons. After introduction of coated rGO nanolayers, the formation rate of H₂ product decreases remarkably, indicating that the coated rGO nanolayers can promote photocatalytic CO₂ reduction, which may be related to its adsorption and activation capacity for CO₂.

As shown in Table 1, the rGO-based catalysts show the high selectivity of CO₂ reduction (S_{CO2}), and the S_{CO2} value of Ag₄/Cu₂O@rGO catalyst is 94.3%. The selectivity of CH₄ (S_{CH4}) and CO (S_{CO}) products during photocatalytic CO₂ conversion are also exhibited in Table 1 and Fig. 5C. Supported Ag NPs on Cu₂O octahedral nanocrystals are conducive to enhance the selectivity of CO₂ photoreduction into CH₄. The S_{CH4} values over Ag_n/Cu₂O@rGO catalysts are more than 90%, while the value of Cu₂O@rGO catalyst is only 47.6%. It suggests that the synergy effect of Ag NPs and rGO nanolayers plays an important role during selective catalytic CO₂ photoreduction into CH₄ product, which is dependent on the increasing surface enrichment density of photo-generated electrons by supported Ag NPs and activated CO₂ by rGO nanolayers. In addition, it should be pointed out that the reaction of photocatalytic CO₂ conversion with H₂O is accompanied by the formation of O₂. For Ag₄/Cu₂O@rGO catalyst, the formation rate of O₂ is 182.3 μmol g⁻¹ h⁻¹, which is slightly higher than the theoretical value (169.8 μmol g⁻¹ h⁻¹) based on other products by this formula: $n(\text{O}_2) = [$

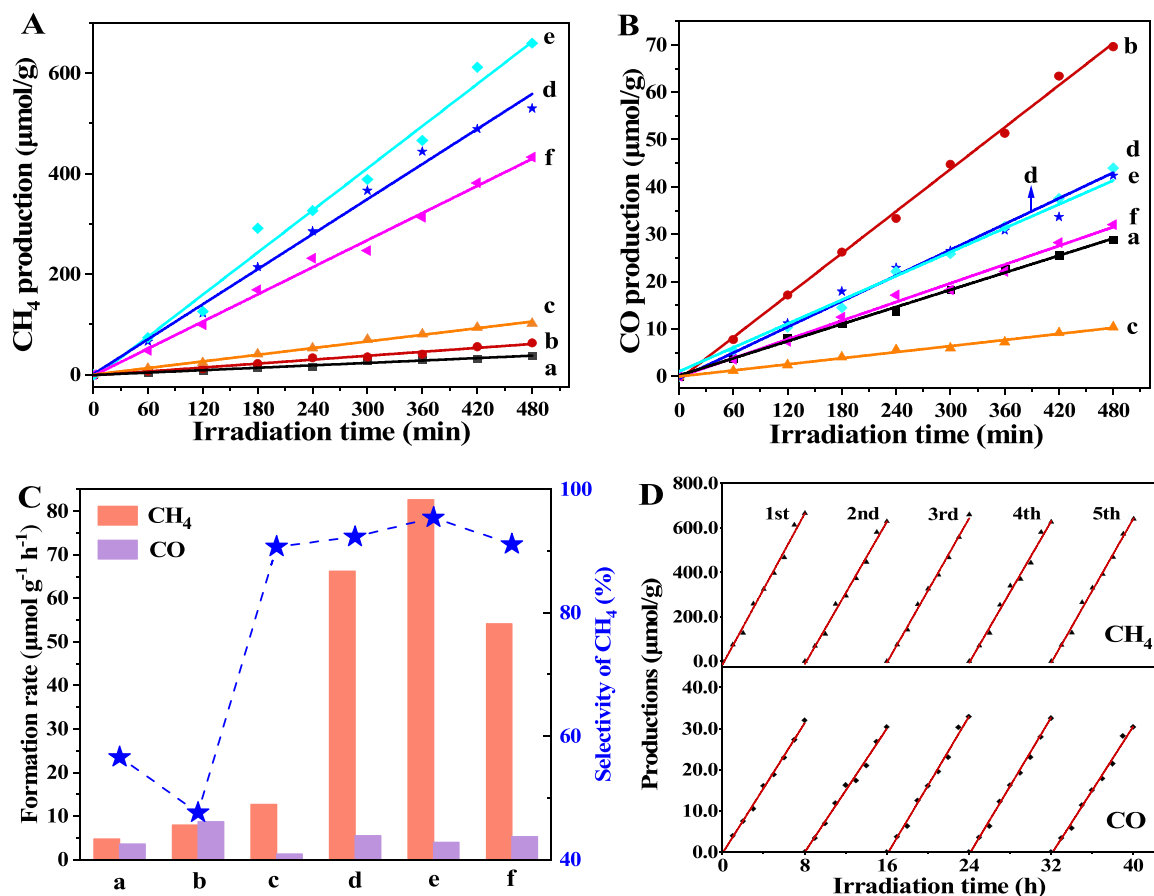


Fig. 5. The evolution of CH₄ (A) and CO (B) products during photocatalytic CO₂ reduction over time; (C) Product yields of CH₄ and CO products and the selectivity of CH₄ product over the prepared catalysts. (D) Cycling tests for CO₂ photoreduction to CO and CH₄ over Ag₄/Cu₂O@rGO photocatalyst under the same as reaction conditions. (a) Cu₂O; (b) Cu₂O@rGO; (c) Ag/Cu₂O; (d) Ag₂/Cu₂O@rGO; (e) Ag₄/Cu₂O@rGO; (f) Ag₆/Cu₂O@rGO.

Table 1

The formation rates, the selectivity of CO and CH₄ products, the selectivity for CO₂ reduction and the apparent quantum efficiency (AQE) for photocatalytic conversion of CO₂ with H₂O over Cu₂O, Cu₂O@rGO, Ag/Cu₂O, Ag₂/Cu₂O@rGO, Ag₄/Cu₂O@rGO and Ag₆/Cu₂O@rGO catalysts.

Sample	Formation rate [μmol g ⁻¹ h ⁻¹] ^a				S _{CO} (%) ^b	S _{CH₄} (%) ^b	S _{CO₂} (%) ^c	AQE (%) ^d
	CH ₄	CO	H ₂	O ₂				
Cu ₂ O	4.7	3.6	5.6	N.d. ^e	43.4	56.6	59.7	0.08
Cu ₂ O@rGO	7.9	8.7	1.4	29.7	52.4	47.6	92.4	0.23
Ag/Cu ₂ O	12.7	1.3	56.8	63.2	9.3	90.7	44.5	0.56
Ag ₂ /Cu ₂ O@rGO	66.2	5.5	12.6	150.4	7.7	92.3	85.1	1.09
Ag ₄ /Cu ₂ O@rGO	82.6	4.0	5.2	182.3	4.6	95.4	94.3	1.26
Ag ₆ /Cu ₂ O@rGO	54.1	5.3	13.2	129.7	8.9	91.1	81.8	0.85

^a Reaction conditions: catalyst sample, 0.15 g; H₂O, 1.5 mL; CO₂ pressure, 0.1 MPa; irradiation time, 8 h; reaction temperature, 5 °C.

^b Selectivity (%) = $n(\text{CO})$ or $n(\text{CH}_4)/[n(\text{CO}) + n(\text{CH}_4)] \times 100\%$.

^c Selectivity for CO₂ reduction to CO and CH₄: Selectivity (%) = $[2n(\text{CO}) + 8n(\text{CH}_4)]/[2n(\text{CO}) + 8n(\text{CH}_4) + 2n(\text{H}_2)] \times 100\%$.

^d The value of AQE is calculated by this equation: $\text{AQE} = [\text{Number of CO} \times 2 + \text{Number of CH}_4 \times 8]/[\text{Number of incident photons}] \times 100\%$.

^e Not determined.

$2n(\text{CO}) + 8n(\text{CH}_4) + 2n(\text{H}_2)]/4$. The other as-prepared catalysts are calculated by the above formula, and their formation rates of O₂ product are in accordance with the electron balance in theory.

To further investigate the utilization efficiency of light energy, the apparent quantum efficiency (AQE) of the catalysts represents the conversion efficiency of light-chemical energy. The AQE value is calculated by this equation: $\text{AQE} = [\text{Number of CO} \times 2 + \text{Number of CH}_4 \times 8]/[\text{Number of incident photons}] \times 100\%$, and the results are displayed in Table 1. Compared with bare Cu₂O and binary Cu₂O@rGO, Ag/Cu₂O catalysts, the AQE values of ternary Ag_n/Cu₂O@rGO catalysts are significantly increased. Ag₄/Cu₂O@rGO catalyst has the largest AQE

value (1.26%), which is 10.6-fold of bare Cu₂O catalyst (0.08%). It further achieves one in-depth understanding of Ag_n/Cu₂O@rGO catalysts with suitable Ag loading, which is of great significance for improving the capture and utilization of solar energy. To further explore the stability of Ag_n/Cu₂O@rGO catalysts, the consecutive cycles (five times) during photocatalytic CO₂ conversion were carried out under the same as the conditions of activity test. Fig. 5D exhibits the evolution of CO and CH₄ products during cycling tests for photocatalytic CO₂ reduction over time over Ag₄/Cu₂O@rGO photocatalyst. It is found that the formation rates of CO and CH₄ products have not significant change, indicating that Ag_n/Cu₂O@rGO catalysts have good photocatalytic

stability for CO₂ reduction. Fig. S5 show the SEM and TEM images of Ag₄/Cu₂O@rGO photocatalyst after the five-cycle tests in order to investigate their structure stability. It is observed that the nanostructures of Cu₂O octahedral nanocrystal, supported Ag NPs and coated rGO nanolayers have not changed obviously. Compared with the fresh sample, the XRD (Fig. S6) and XPS (Fig. S7) spectra of used Ag₄/Cu₂O@rGO catalyst after five cycles have not significant change. Combined with results of SEM, TEM, XRD and XPS, it suggests that Ag₄/Cu₂O@rGO catalyst possess excellent structural stability during photocatalytic CO₂ reduction with H₂O. As we all know, the accumulation of photogenerated holes is the main reason of Cu₂O photocorrosion, the modified Cu₂O (Ag_n/Cu₂O@rGO) catalyst accelerates the consumption of h⁺ and promotes the generation of O₂ [34]. And the protective effect of coated rGO nanolayers can restrain the oxidation of Cu₂O nanocrystals, which is beneficial to maintain the stability of Ag_n/Cu₂O@rGO catalysts.

In addition, to confirm the CO₂ as the only carbon resources for carbon-containing products, a series of experiments were carried out under conditions of normal activity tests with one parameter missing, such as, in the absence of CO₂ reactant, the light irradiation or the catalysts. The carbon-containing products (CO and CH₄) during blank experiments have been undetected, indicating that the light irradiation and the catalysts are essential condition for photocatalytic CO₂ reduction. To further tracing the carbon and hydrogen sources in CO and CH₄

products, the isotopic labeling experiment with D₂O and ¹³CO₂ reactants over Ag₄/Cu₂O@rGO catalyst was carried out under conditions of the same activity tests. Fig. S8 exhibits the products of photocatalytic ¹³CO₂ reduction with D₂O analyzed by GC-MS after visible light irradiation for 8 h. As displayed in Fig. S8a, three peaks in GC signal are observed during CO₂ photoreduction, which are ascribed to the composition of CO, CH₄ and CO₂. Each peak in GC signal is further analyzed by MS device, and the results are exhibited in Figs. S8(b-d). As exhibited in Fig. S8b, the signal intensity of *m/z* at 29 corresponding to ¹³CO component is higher than that of *m/z* at 45 (¹³CO₂), suggesting that ¹³CO product is derived from the ¹³CO₂ photoconversion rather than the fragmentary peak of ¹³CO₂ reactant. All kinds of *m/z* signals in the range of 13–21 are noted in Fig. S8c, which are assigned to the fragmentary peaks of ¹³CD₄ molecular derived from photocatalytic ¹³CO₂ reduction with D₂O. But the signal of ¹²CD₄ product (*m/z* = 20) is not observed, suggesting that ¹³CO₂ is the only carbon source of hydrocarbon products for catalytic CO₂ photoreduction. In Fig. S8d, the main signal of ¹³CO₂ reactant (*m/z* = 45) is found, and the fragmentary peaks of ¹³CO₂ (*m/z* = 13–30) are also observed. Based on the results of ¹³C and ²H(D) isotopic labeling test, it indicates that the carbon and hydrogen element in the formation products are originated from CO₂ and H₂O reactants. In summary, Ag_n/Cu₂O@rGO catalysts have the satisfactory potency during photocatalytic CO₂ conversion with H₂O into solar fuel in practical application.

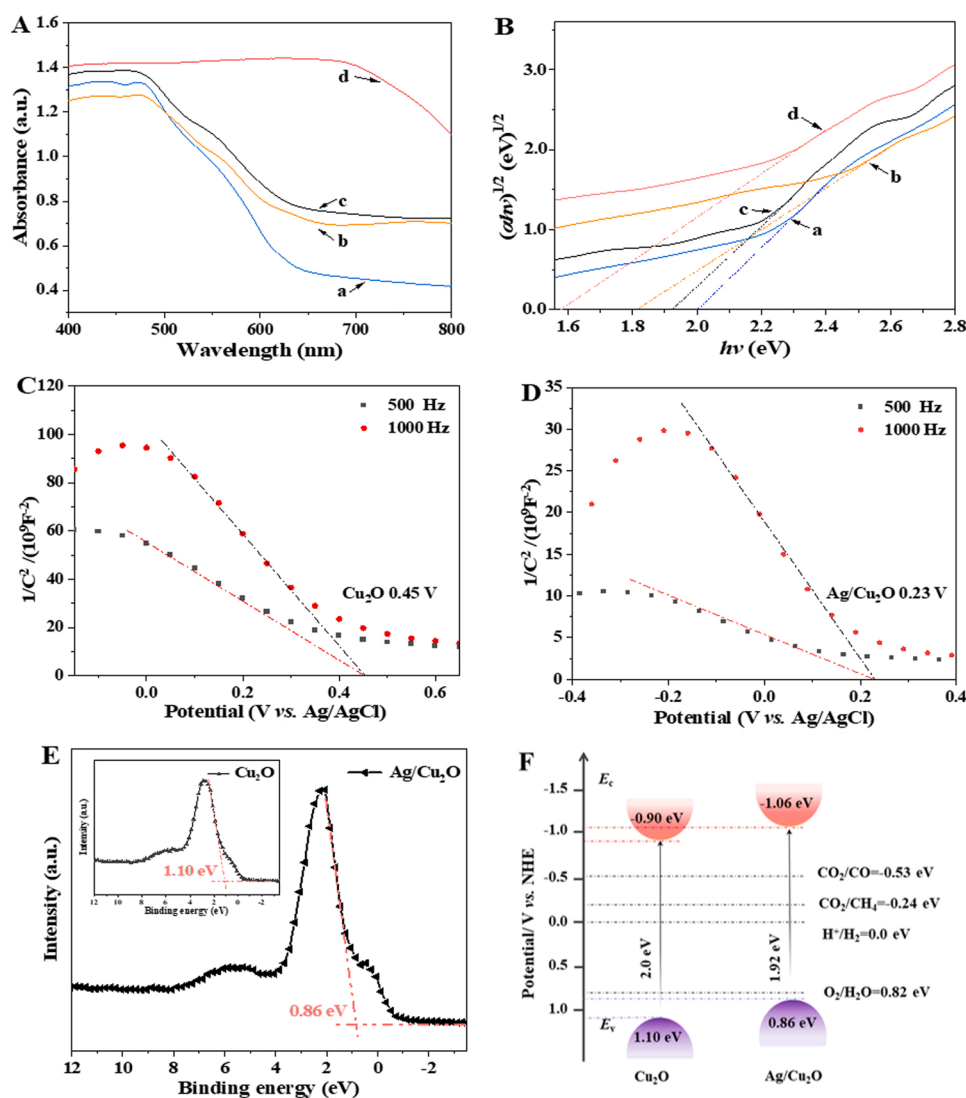


Fig. 6. UV-vis spectra (A) and E_g estimated by plotting $(\alpha h\nu)^{1/2}$ versus $h\nu$ (B) over Cu₂O, Cu₂O@rGO, Ag/Cu₂O and Ag/Cu₂O@rGO catalysts; The Mott-Schottky plots of Cu₂O (C) and Ag/Cu₂O (D) catalysts at different frequencies (500, 1000 Hz) obtained by plotting the variation of interfacial capacitance (C in the ordinate); (E) Valence band XPS spectra of Cu₂O and Ag/Cu₂O catalysts; (F) Schematic illustration of energy band structure for Cu₂O and Ag/Cu₂O catalysts. (a) Cu₂O; (b) Cu₂O@rGO; (c) Ag/Cu₂O; (d) Ag/Cu₂O@rGO.

3.3. Characterizations of photoelectrical properties

The UV-vis DRS spectra of Cu_2O , $\text{Ag}/\text{Cu}_2\text{O}$, $\text{Cu}_2\text{O}@r\text{GO}$ and $\text{Ag}_n/\text{Cu}_2\text{O}@r\text{GO}$ catalysts were carried out to explore their optical absorption properties in the range of 400–800 nm, and the results are displayed in Fig. 6 (A–B). As can be seen from Fig. 6A, the absorption edge of bare Cu_2O catalyst is approximately 650 nm. Compared with bare Cu_2O catalyst, $\text{Cu}_2\text{O}@r\text{GO}$ and $\text{Ag}/\text{Cu}_2\text{O}$ catalysts exhibit a slight expansion of the light absorption edges, indicating that the introduction of rGO or Ag NPs plays a critical role in improving their absorption capacity of visible light. Notably, the absorption edge for $\text{Ag}/\text{Cu}_2\text{O}@r\text{GO}$ catalyst in the range of visible light has the significant red shift exhibited in Fig. 6A. Both the enhancement of $\pi-\pi^*$ conjugation effect by rGO and the plasmon resonance effect of Ag NPs are indispensable for the change [20,35]. Thus, the ternary rGO-Ag- Cu_2O heterojunction with synergistic effect can enhance the utilization efficiency of light energy to a certain extent, which provides new opportunities to improve the photocatalytic performance for CO_2 conversion. Fig. 6B depicts the energy gap for as-prepared catalysts according to the formula $(\alpha h\nu)^{1/2} = A(h\nu - E_g)$, where the α is absorption coefficient, the $h\nu$ is the absorbed photon energy of 40.0 eV, the A is a constant, $1/2$ represents indirect band gap semiconductor, and the E_g refers to the bandgap energy. As exhibited in Fig. 6B, the band gap of $\text{Ag}/\text{Cu}_2\text{O}$ is calculated as 1.92 eV, while that of bare Cu_2O catalyst is 2.0 eV, indicating that the impurity state of Ag component is in the band gap, which can effectively reduce the band gap. And on the other hand, it promotes the transition of electrons: the electrons at the top of valence band can firstly transfer to the impurity state in the band gap, and then continue to transfer to the bottom of conduction band [36]. Thus, the absorption of visible light is significantly improved by ternary rGO-Ag- Cu_2O heterojunction.

The flat band potential (E_{fb}) is an important parameter of the semiconductor system, and its value can be employed to determine the energy level structure of the semiconductor, which is very crucial for the development and utilization of related photocatalytic semiconductors with solar energy. The Mott-Schottky (MS) is suitable for testing two-phase composite band structures [37]. The flat band potentials of Cu_2O and $\text{Ag}/\text{Cu}_2\text{O}$ catalysts were pinpointed by the Mott-Schottky plots, and the results are shown in Fig. 6C and 6D. The E_{fb} value was obtained by processing the linear relationship between the reciprocal of the square of the interfacial capacitance ($1/C^2$) and the applied potential. The E_{fb} values of Cu_2O and $\text{Ag}/\text{Cu}_2\text{O}$ catalysts were measured to be 0.45 V and 0.23 V versus Ag/AgCl electrode, respectively. The obtained potentials could be converted into normal hydrogen electrode (NHE) potentials by the following formula [38]:

$$E_{NHE} = E_{AgCl} + E_{AgCl}^0 + 0.059 \text{ pH} \quad (2)$$

where E_{AgCl}^0 represents the standard potential of Ag/AgCl (0.1976 V) at $\text{pH} \approx 7$. The Cu_2O with a negative slope confirms that it is a p-type semiconductor. It is well known that the flat potential of doped p-type semiconductor is equal to the valence band edge potential [39]. Hence, the calculated VB edge positions of Cu_2O and $\text{Ag}/\text{Cu}_2\text{O}$ catalysts were estimated to be 1.06 and 0.84 V versus NHE. To further investigate the valence band edge potentials of Cu_2O and $\text{Ag}/\text{Cu}_2\text{O}$ catalysts, Fig. 6E reports the valence band X-ray photoelectron spectroscopy (VB-XPS). It is beneficial to in-depth understanding the influence of the energy band structure of the semiconductor on the photocatalytic activity for CO_2 reduction [40]. The maximum valence band energy of Cu_2O and $\text{Ag}/\text{Cu}_2\text{O}$ catalysts occurred at 1.10 and 0.86 eV, respectively, which are almost consistent with the observation of Mott-Schottky test. Based on the results of the UV-vis, Mott-Schottky and VB-XPS, it could be concluded that the minimum conduction band energy of Cu_2O and $\text{Ag}/\text{Cu}_2\text{O}$ catalysts is determined to be -0.90 and -1.06 eV, respectively. As shown in Fig. 6E, the schematic illustration shows clearly the influence of introducing Ag NPs on the energy band structure of Cu_2O and $\text{Ag}/\text{Cu}_2\text{O}$ catalysts. After introduction of supported Ag NPs,

$\text{Ag}/\text{Cu}_2\text{O}$ catalyst exhibits the narrower band gap and more negative reduction potential compared with Cu_2O catalyst, which is advantageous to realize CO_2 conversion under visible light irradiation.

The reaction nature of photocatalytic CO_2 reduction is the photoelectric conversion process; thus, the electrochemical impedance spectroscopy (EIS) and transient photocurrent responses were carried out to explore photoelectric conversion capability and carrier separation efficiency, and the results are exhibited in Fig. 7. As depicted in Fig. 7A, a large semicircle domain of bare Cu_2O nanocrystal represents the relatively high charge transfer resistance (R_{ct}). The smaller the radius of the curve is, the smaller the R_{ct} is. After introduction of rGO or/and Ag NPs on the surface of Cu_2O octahedral nanocrystals, the R_{ct} values of $\text{Cu}_2\text{O}@r\text{GO}$ and $\text{Ag}/\text{Cu}_2\text{O}$ catalysts decrease obviously, which is attributed to the acceleration of charge transfer at the interface of $\text{Cu}_2\text{O}@r\text{GO}$ and $\text{Ag}/\text{Cu}_2\text{O}$ catalysts. Compared with $\text{Cu}_2\text{O}@r\text{GO}$ catalyst, $\text{Ag}/\text{Cu}_2\text{O}$ catalyst has the more effective separation efficiency of photogenerated carriers, which may be ascribed to good conductivity of Ag NPs. The result is consistent with the conclusion of LSV test (Fig. S9). It is worth noting that the R_{ct} values of $\text{Ag}_n/\text{Cu}_2\text{O}@r\text{GO}$ catalysts with ternary rGO-Ag- Cu_2O heterojunction further decreased remarkably, indicating that the synergistic effect of ternary rGO, Ag NPs and Cu_2O components can effectively improve the transfer and separation efficiency of photoinduced carriers.

As shown in Fig. 7B, the transient photocurrent responses were recorded by switching the visible-light on-off for five cycles. Generally,

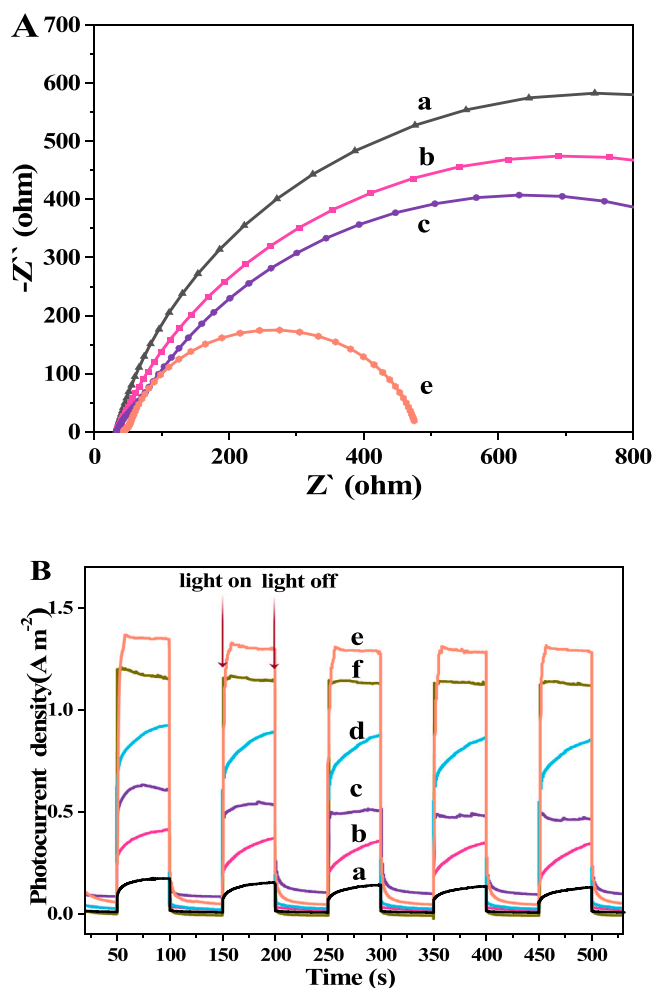


Fig. 7. Electrochemical impedance spectroscopy (EIS) (A) and transient photocurrent responses (B) of Cu_2O , $\text{Cu}_2\text{O}@r\text{GO}$, $\text{Ag}/\text{Cu}_2\text{O}$ and $\text{Ag}_n/\text{Cu}_2\text{O}@r\text{GO}$ catalysts. (a) Cu_2O ; (b) $\text{Cu}_2\text{O}@r\text{GO}$; (c) $\text{Ag}/\text{Cu}_2\text{O}$; (d) $\text{Ag}_2/\text{Cu}_2\text{O}@r\text{GO}$; (e) $\text{Ag}_4/\text{Cu}_2\text{O}@r\text{GO}$; (f) $\text{Ag}_6/\text{Cu}_2\text{O}@r\text{GO}$.

the larger the photocurrent density is, the higher the carrier mobility is. The photocurrent density of $\text{Ag}_4/\text{Cu}_2\text{O}@r\text{GO}$ catalyst dramatically increases to $1.35 \text{ A}\cdot\text{m}^{-2}$ in comparison with $0.17 \text{ A}\cdot\text{m}^{-2}$ of Cu_2O catalyst, suggesting that the $\text{Ag}_n/\text{Cu}_2\text{O}@r\text{GO}$ catalysts have good the separation efficiency of photoinduced electron-hole pairs, which is responsible for enhancing photocatalytic activity. It was demonstrated that supported Ag NPs act as electron traps can capture electrons and prevent the recombination of photogenerated electron-hole pairs [41]. However, with the same content of Cu_2O nanocrystals and coated rGO nanolayers, the photocurrent density of $\text{Ag}_6/\text{Cu}_2\text{O}@r\text{GO}$ catalyst is lower than that of $\text{Ag}_4/\text{Cu}_2\text{O}@r\text{GO}$ catalyst. It indicates that an appropriate amount of Ag NPs is more conducive to the improvement of the separation efficiency of photogenerated electron-hole pairs, which is consistent with the results of Surface photovoltage (SPV) characterization (Fig. S11). Based on the results of EIS and transient photocurrent responses, the coated rGO nanolayers in the $\text{Ag}_n/\text{Cu}_2\text{O}@r\text{GO}$ catalysts can improve the separation efficiency of photogenerated electron-hole pairs, indicating that rGO nanolayers is used to an electron reservoir. Thus, the rGO nanolayers and Ag NPs in $\text{Ag}_n/\text{Cu}_2\text{O}@r\text{GO}$ catalysts play the crucial role of photogenerated electron acceptor. $\text{Ag}_n/\text{Cu}_2\text{O}@r\text{GO}$ catalysts, which combined with the efficient separation efficiency of carriers and the prolonged lifetime of photogenerated electrons, exhibit high catalytic performances during visible light-driven CO_2 conversion with H_2O into CH_4 .

3.4. Photocatalytic mechanism for CO_2 reduction

The discovering transfer pathways of photogenerated charge is very essential for in-depth understanding of photocatalytic mechanism for CO_2 conversion into CH_4 product. Fig. 8 shows the transfer pathways of photogenerated charge. As illustrated in Fig. 8A, it is well known that Cu_2O nanocrystal is a p-type semiconductor with larger work function (5.30 eV) in comparison with that of Ag (4.26 eV) [42]. As shown in Fig. 8B, after introduction of supported Ag NPs on Cu_2O nanocrystals, the electrons of Ag NPs will be spontaneously transferred to Cu_2O nanocrystal through the contact interface until the Fermi level of the Ag/ Cu_2O catalyst reaches the same new level ($\sim -4.78 \text{ eV}$). Interestingly, the internal electric field is formed at the interface between supported Ag NPs and Cu_2O nanocrystals. During the formation process of internal electric field, Cu_2O nanocrystals can get electrons and is negatively charged, while Ag NPs are positively charged. Thus, the energy band edge of Cu_2O nanocrystals bends downward, which is attributed to the surface accumulation of electrons.

As shown in Fig. 8C, the unstable light-excited electrons will react or transfer to lower energy band positions under visible-light irradiation. The photogenerated electrons in conduction band of Cu_2O nanocrystals are excited into the valence band, and then rapidly injected into supported Ag NPs. The spatial separation of photogenerated electrons and holes can greatly alleviate the recombination of electron-hole pairs. Thus, the photoelectrons generated by light-excited Cu_2O are captured

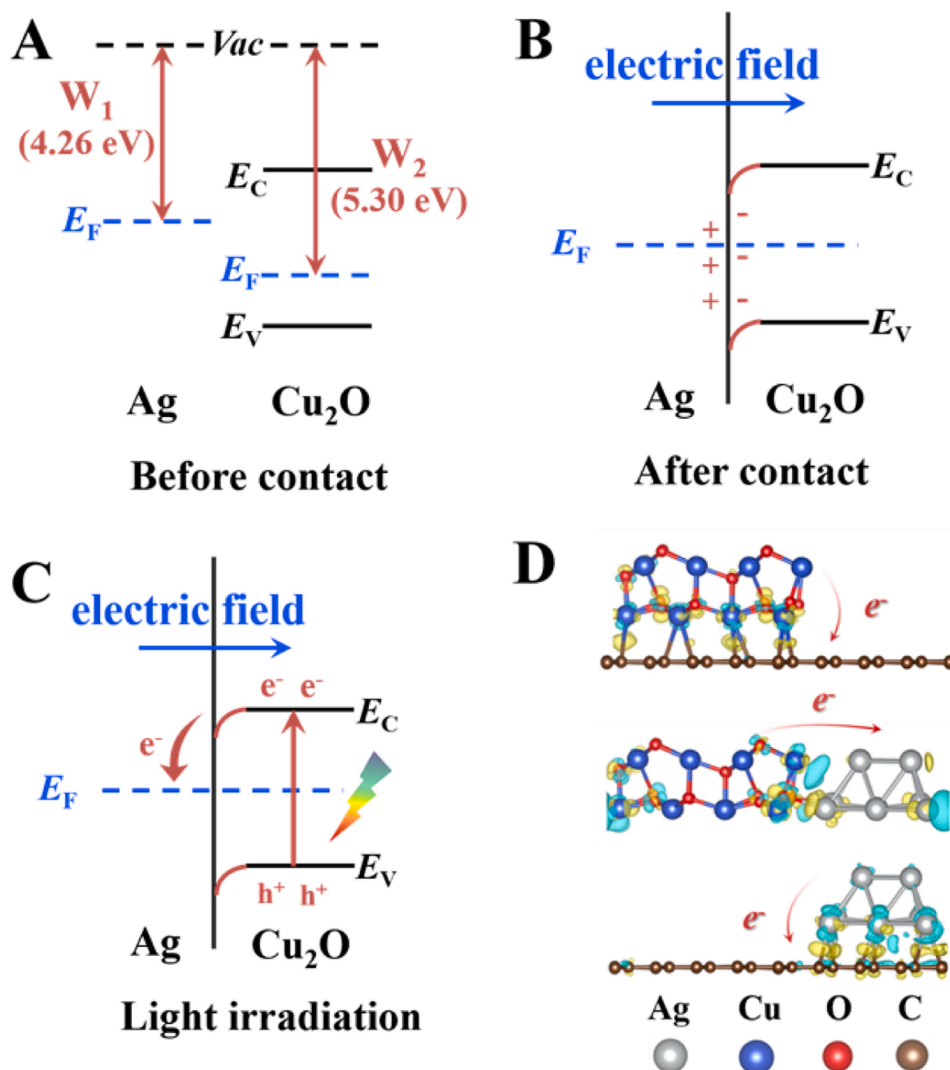


Fig. 8. The transfer pathways of photogenerated charge over the catalysts. (A) The work functions of Ag NPs and Cu_2O nanocrystals; (B) The adjustment of the Fermi level, the formation of electric field and the bending of band edge of Cu_2O in Ag/ Cu_2O catalysts; (C) The transfer of photogenerated charges over Ag/ Cu_2O catalyst under light irradiation; (D) The charge difference distribution between adsorbed CO_2 and Ag/ $\text{Cu}_2\text{O}@r\text{GO}$ catalysts (Yellow: charge accumulation; Blue: depletion). (For interpretation of the references to colour in this figure, the reader is referred to the web version of this article.)

by Ag NPs, and the active photoelectrons are enriched on the Ag NPs surface, which can not only provide necessary conditions for CO₂ conversion, but also promotes the enhancing surface adsorption and activation properties for CO₂. Simultaneously, the work function of rGO nanolayer (~4.40 eV) is lower than that of Cu₂O nanocrystals, thus, the coated rGO nanolayers might also act as the role of electron trap [43]. In order to further confirm the charge transfer mechanism, the DFT calculations were carried out to reveal the charge density differences in Ag_n/Cu₂O@rGO catalyst. As shown in Fig. 8D, the electron transfer processes are described by charge difference distribution where charge accumulation is shown in yellow and charge depletion in blue. The presence of Ag NPs and rGO nanolayers could result in charge transfer from Cu₂O to the surrounding Ag and C atoms, which leads to charge enrichment on the Ag NPs and rGO nanolayers. It is worth noted that the charge-enriched sites at the interface between Ag NPs and rGO nanolayers can act as the capture sites for photogenerated electrons, which is conducive to stabilizing the intermediates produced by the CO₂ reduction reaction. The ternary heterojunctions are formed at the interface between Ag NPs, Cu₂O nanocrystals and rGO nanolayers, suggesting that the strong electronic coupling of ternary rGO-Ag-Cu₂O heterojunction is beneficial to the formation of an efficient charge transfer pathway, which can strongly inhibit the recombination of photogenerated electron-hole pairs. After the introduction of Ag NPs and rGO nanolayers, the PL signal (Fig. S10) further decreases, indicating that Ag NPs and rGO can serve as the “electron reservoir” to trap the photogenerated electrons and restrain the recombination of photogenerated carriers. This unique charge transfer mechanism strengthens the redox ability of the Ag/Cu₂O@rGO catalyst, and provides strong driving force for selective catalytic CO₂ photoreduction with H₂O into CH₄.

On the basis of the above results, the reaction mechanism for photocatalytic CO₂ conversion with H₂O over the Ag/Cu₂O@rGO catalysts is proposed. The Ag/Cu₂O@rGO photocatalyst with a narrower band gap can achieve higher photon enrichment. Under light irradiation, Cu₂O nanocrystals can absorb the visible light and are excited to formation of conduction band and valence band. The photogenerated electrons located at conduction band can rapidly transfer to supported Ag NPs and rGO nanolayers to realize the catalytic CO₂ reduction reaction. Based on the results of EIS (Fig. 7A) and transient photocurrent responses (Fig. 7B), it is confirmed that the Ag_n/Cu₂O@rGO catalysts promote the separation efficiency and rapid transport of photoinduced charge. And the oxidation reaction of H₂O occurred at the valence band position of Cu₂O nanocrystals, which can result in the formation of O₂. In addition, the effective consumption of photogenerated holes can restrain the photo-corrosion of Cu₂O nanocrystals, which is one of the reasons for keeping the high stability of the catalyst [34].

The nature of photocatalytic CO₂ conversion is one typical heterogeneous catalysis reaction occurring in the interface of gaseous reactants and solid catalysts. Thus, the surface adsorption and activation properties of the catalysts for CO₂ are also crucial to improve the selective catalytic performance of CO₂ photoreduction into CH₄. To explore the adsorption and activation capacity of the catalysts for CO₂ reactant, the CO₂-adsorption DRIFTS over Cu₂O, Cu₂O@rGO and Ag₄/Cu₂O@rGO catalysts were carried out, and the results are shown in Fig. 9 A. It is found that the adsorption for CO₂ over the as-prepared catalysts is mainly physical adsorption, and two absorption peaks are observed at 2338 and 2360 cm⁻¹, which are ascribed to ν₃(CO₂) absorption of the surface CO₂ molecular [44]. And the deposition of Ag NPs on the surface of Cu₂O nanocrystals has slight boost the peak intensity of CO₂ adsorption, while the rGO nanolayers coated on Ag/Cu₂O can significantly improve the peak intensity of CO₂ adsorption, indicating that rGO nanolayers have the remarkable property for improving the ability of adsorption and activation for CO₂ reactant, which is of great importance to the subsequent reaction of CO₂ conversion into CH₄ product. Thus, the surface enrichment of CO₂ adsorption over Ag_n/Cu₂O@rGO catalysts is beneficial to enhancing the photocatalytic selectivity for CO₂ conversion into CH₄ in comparison with that for H₂O photoreduction.

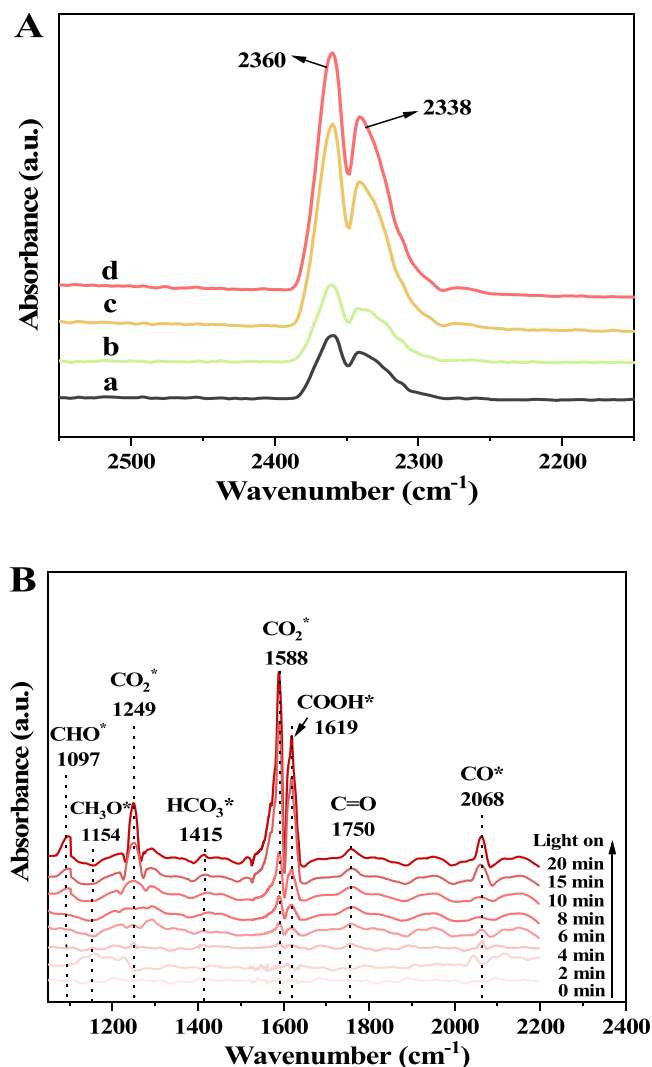


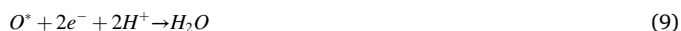
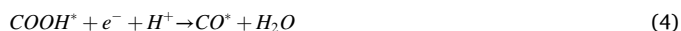
Fig. 9. (A) CO₂-adsorption DRIFT spectra of the prepared catalysts (the adsorption curves are all selected in the state of adsorbing CO₂ for 20 min in the dark); (B) In situ DRIFT spectra over Ag₄/Cu₂O@rGO catalyst for visible light-driven CO₂ reduction. (a) Cu₂O; (b) Ag/Cu₂O; (c) Cu₂O@rGO; (d) Ag₄/Cu₂O@rGO.

And combined with the capture and enrichment properties of photo-generated electrons by supported Ag NPs and coated rGO nanolayers, Ag_n/Cu₂O@rGO catalysts show the high catalytic activity and selectivity during CO₂ conversion with H₂O into CH₄ product, which is confirmed by their photocatalytic performances shown in Table 1.

To further reveal the reaction intermediates and reaction pathways during the photocatalytic CO₂ conversion, the in-situ DRIFT spectra of Ag₄/Cu₂O@rGO catalyst were carried out, and the results are displayed in Fig. 9B. Under continuous light irradiation, the absorption peaks at 1249 and 1588 cm⁻¹ are ascribed to the bending vibration of the CO₂* radical in dynamic evolution spectra of surface intermediates [45,46]. Notably, the appearance of CO₂* radical indicates that CO₂ could be adsorbed and activated on the surface of Ag₄/Cu₂O@rGO catalyst. It has shown in the previous reports that the light irradiation is crucial to the activation of CO₂ into CO₂* through the formation of photogenerated carriers [47]. The absorption peak centered at 1619 cm⁻¹ is ascribed to symmetric stretching of COOH* intermediate [48], and its intensity increases with the prolongation of illumination time. The absorption peaks located at 1097 and 1154 cm⁻¹ are assigned to symmetric stretching of CHO* and OCH₃* species, respectively. The CHO* species is considered to be the crucial intermediate for selective photocatalytic

CO₂ reduction to CH₄ product [49]. The surface density of CHO* intermediate on the surface of Ag_n/Cu₂O@rGO catalysts increases under light irradiation, and it is further protonated to boost the formation of CH₄ product. It suggests that supported Ag NPs could effectively capture photoelectrons, which can facilitate the rapid injection of electrons and protons into the CO₂ molecules adsorbed by rGO nanolayers to generate CHO* intermediate.

In addition, there are three time-dependent absorption peaks of DRIFTS located at 1415, 2068 and 1750 cm⁻¹, which are ascribed to the symmetrical stretching vibration peak of HCO₃* species, the stretching vibration peak of CO* intermediate and the stretching vibration peak of C=O bond, respectively [50]. The formation of CO* intermediate is ascribed to the one-step protonation of COOH* species, and the CO* intermediate on the surface of Ag₄/Cu₂O@rGO catalyst will be followed by two competitive key reaction steps: i) The surface CO* species is rapidly protonated to further generate CHO* intermediates, which results in the formation of CH₄; ii) The surface CO* species is not transformed to other transition states, but generates CO product through the desorption process, which is responsible for the formation of CO product during photocatalytic CO₂ reduction. Based on the results of in-situ DRIFT spectra, the reaction pathways for photocatalytic CO₂ conversion into CO and CH₄ over Ag₄/Cu₂O@rGO catalyst are listed as follows:



Combined with the results of DFT calculations, the reaction steps during photocatalytic CO₂ reduction are proposed, and the schematic of photocatalytic mechanism for CO₂ reduction over the catalysts is shown in Fig. 10: a large amount of gaseous CO₂ molecule could first be adsorbed by the coated rGO nanolayers with an adsorption energy of -0.36 eV (the details are in the supporting information, Table S3), and the gaseous H₂O molecule can also be adsorbed at the Cu₂O site with an adsorption energy of -0.53 eV, which are further activated and can react with photogenerated hole to generate O₂ product. The reaction pathways of Ag_n/Cu₂O@rGO catalysts during photocatalytic CO₂ reduction follow the route of COOH* intermediate. The enrichment of surface photogenerated electrons at the interface between supported Ag NPs and coated rGO nanolayers can effectively stabilize the reaction intermediates, which results in the enhancing photocatalytic activity [51]. Under the light irradiation, supported Ag NPs in the Ag_n/Cu₂O@rGO catalysts can effectively capture photoelectrons derived from excited Cu₂O nanocrystals, which results in facilitating the rapid injection of electrons and protons into the CO₂ molecules adsorbed by coated rGO nanolayers. The activated CO₂* species obtained by the activation of CO₂ can undergo consecutive proton absorption processes to generate the crucial COOH* and CO* intermediate, and the formation of COOH* intermediate is the rate-limiting step. It is well known that the desorption of CO* intermediate is an endothermic process, while the process of protonation is exothermic and spontaneous. The multiple active sites will induce strong adsorption of CO* species, which is beneficial for further protonation to CH₄ product [52]. The desorption energy of CO* (0.065 eV) is significantly higher than the formation of CHO* (-0.358 eV) with respect to the calculated Gibbs free energy, indicating that the CO* intermediate is inclined to continue protonation to form CHO* intermediate, which is responsible for the high selectivity (95.4%) of CH₄ product over Ag₄/Cu₂O@rGO catalysts during photocatalytic CO₂ reduction. In addition, the C-O bond in the OCH₃* radical is weakened and easily broken by virtue of the strong hybridization between the d-orbit of Ag (charge-enriched site) and the p-orbit of O atoms (O atom of OCH₃*), which is also in favor of the formation of CH₄

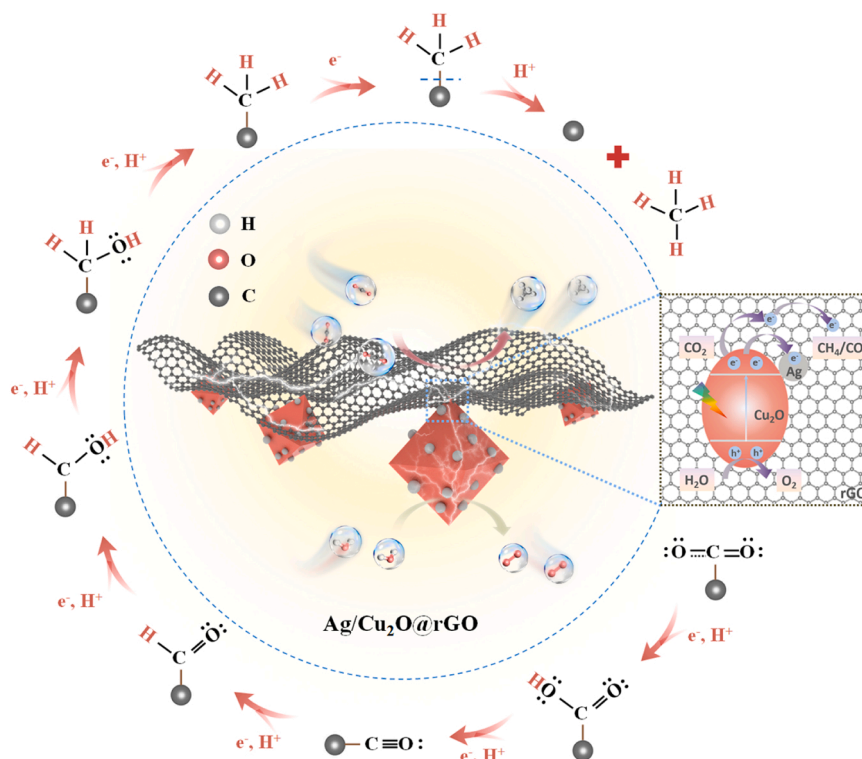


Fig. 10. Schematic of the mechanism for CO₂ photoreduction into CH₄ over Ag/Cu₂O@rGO catalyst.

product. Thus, Ag_n/Cu₂O@rGO catalysts improve the activity and selectivity for photocatalytic reduction of CO₂ with H₂O into CH₄ product, and it would have bright prospects in photocatalysis.

4. Conclusion

A novel core-shell structured Ag_n/Cu₂O@rGO catalysts were successfully constructed via the method of water bath combining with gas-bubbling-assisted membrane reduction. Supported Ag NP in the Ag_n/Cu₂O@rGO catalysts is crucial to enriching the photoelectrons originated from visible light-excited Cu₂O octahedral nanocrystals, which is beneficial for promoting the separation efficiency of photogenerated electron-hole pairs. The coated rGO nanolayer on the surface of Ag/Cu₂O has the surface extended π bond for enhancing the adsorption-activation property for CO₂ reactant. The ternary rGO-Ag-Cu₂O heterojunction in Ag_n/Cu₂O@rGO catalysts can realize the simultaneous improvement of the absorption efficiency of visible light, the separation efficiency of photogenerated electron-hole pairs and the adsorption-activation property for CO₂ reactant. Ag_n/Cu₂O@rGO catalysts exhibit excellent performance during selective photocatalytic CO₂ conversion into CH₄. The highest formation rate and selectivity of CH₄ product over Ag₄/Cu₂O@rGO catalyst is 82.6 $\mu\text{mol g}^{-1} \text{h}^{-1}$ and 95.4%, respectively. Based on the results of in-situ DRIFT spectra and DFT calculations, the catalytic mechanism for CO₂ conversion is proposed: the further protonation of CO* intermediate is key step for selective catalytic CO₂ conversion into CH₄. This work provides new insights into the reaction pathway and mechanism of metal-semiconductor heterogeneous catalysts for selective catalytic CO₂ conversion to C1 chemicals.

CRediT authorship contribution statement

Zhilong Tang: Conceptualization, Methodology, Visualization, Formal analysis, Writing – original draft, Investigation. **Wenjie He:** Software, Formal analysis, Investigation. **Yingli Wang:** Investigation, Data Curation. **Prof. Yuechang Wei:** Conceptualization, Methodology, Investigation, Formal analysis, Writing – review & editing, Supervision, Funding acquisition. **Prof. Xiaolin Yu:** Investigation, Data Curation. **Ph. D Jing Xiong:** Formal analysis, Investigation. **Xiong Wang:** Formal analysis, Visualization. **Prof. Xiao Zhang:** Investigation, Data Curation. **Prof. Zhen Zhao:** Project administration, Data Curation. **Prof. Jian Liu:** Formal analysis, Investigation.

Declaration of Competing Interest

The authors declare that they have no known competing financial interests or personal relationships that could have appeared to influence the work reported in this paper.

Acknowledgements

This work was supported by the National Natural Science Foundation of China (21972166), Beijing Natural Science Foundation (2202045), the Technology Development Program of SINOPEC, China (Grant No. 321101) and National Key Research and Development Program of China (2019YFC1907600).

Appendix A. Supporting information

Supplementary data associated with this article can be found in the online version at [doi:10.1016/j.apcatb.2022.121371](https://doi.org/10.1016/j.apcatb.2022.121371).

References

- [1] C. Wang, Y. Zhao, H. Xu, Y. Li, Y. Wei, J. Liu, Z. Zhao, Efficient Z-scheme photocatalysts of ultrathin g-C₃N₄-wrapped Au/TiO₂-nanocrystals for enhanced visible-light-driven conversion of CO₂ with H₂O, Appl. Catal. B 263 (2020), 118314, <https://doi.org/10.1016/j.apcatb.2019.118314>.

- [2] H. Ge, Y. Kuwahara, K. Kusu, H. Yamashita, Plasmon-induced catalytic CO₂ hydrogenation by a nano-sheet Pt/H_xMoO_{3-y} hybrid with abundant surface oxygen vacancies, J. Mater. Chem. A 9 (2021) 13898–13907, <https://doi.org/10.1039/D1TA02277F>.
- [3] K. Kočí, L. Matějová, O. Kozák, L. Capek, V. Valeš, M. Reli, P. Praus, K. Šafářová, A. Kotarba, L. Obalová, ZnS/MMT nanocomposites: the effect of ZnS loading in MMT on the photocatalytic reduction of carbon dioxide, Appl. Catal. B 158–159 (2014) 410–417, <https://doi.org/10.1016/j.apcatb.2014.04.048>.
- [4] Y. Zhao, Y. Wei, X. Wu, H. Zheng, Z. Zhao, J. Liu, et al., Graphene-wrapped Pt/TiO₂ photocatalysts with enhanced photogenerated charges separation and reactant adsorption for high selective photoreduction of CO₂ to CH₄, Appl. Catal. B 226 (2018) 360–372, <https://doi.org/10.1016/j.apcatb.2017.12.071>.
- [5] C. Wang, X. Liu, W. He, Y. Zhao, Y. Wei, J. Xiong, et al., All-solid-state Z-scheme photocatalysts of g-C₃N₄/Pt/macroporous-TiO₂@carbon for selective boosting visible-light-driven conversion of CO₂ to CH₄, J. Catal. 389 (2020) 440–449, <https://doi.org/10.1016/j.jcat.2020.06.026>.
- [6] C. Dong, Y. Bao, T. Sheng, Q. Yi, Q. Zhu, B. Shen, M. Xing, I.M.C. Lo, J. Zhang, Singlet oxygen triggered by robust bimetallic MoFe/TiO₂ nanospheres of highly efficacy in solar-light-driven peroxymonosulfate activation for organic pollutants removal, Appl. Catal. B 286 (2021), 119930, <https://doi.org/10.1016/j.apcatb.2021.119930>.
- [7] A.M. Abdel-Mageed, M. Büsselmann, K. Wiese, C. Fauth, R.J. Behm, Influence of water vapor on the performance of Au/ZnO catalysts in methanol synthesis from CO₂ and H₂: A high-pressure kinetic and TAP reactor study, Appl. Catal. B 297 (2021), 120416, <https://doi.org/10.1016/j.apcatb.2021.120416>.
- [8] F. Fu, H. Shen, X. Sun, W. Xue, A. Shoneye, J. Ma, L. Luo, D. Wang, J. Wang, J. Tang, Synergistic effect of surface oxygen vacancies and interfacial charge transfer on Fe(III)/Bi₂MoO₆ for efficient photocatalysis, Appl. Catal. B 247 (2019) 150–162, <https://doi.org/10.1016/j.apcatb.2019.01.056>.
- [9] J. Di, X. Zhao, C. Lian, M. Ji, J. Xia, J. Xiong, W. Zhou, X. Cao, Y. She, H. Liu, K. P. Loh, S.J. Pennycook, H. Li, Z. Liu, Atomically-thin Bi₂MoO₆ nanosheets with vacancy pairs for improved photocatalytic CO₂ reduction, Nano Energy 61 (2019) 54–59, <https://doi.org/10.1016/j.nanoen.2019.04.029>.
- [10] X. Xu, K. Teramura, H. Asakura, S. Hosokawa, T. Tanaka, Shift of active sites via in-situ photodeposition of chromate achieving highly selective photocatalytic conversion of CO₂ by H₂O over ZnTa₂O₆, Appl. Catal. B 298 (2021), 120508, <https://doi.org/10.1016/j.apcatb.2021.120508>.
- [11] S. Zhu, X.F. Chen, Z.C. Li, X.Y. Ye, Y. Liu, Y. Chen, L. Yang, M. Chen, D.Q. Zhang, G. S. Li, H.X. Li, Cooperation between inside and outside of TiO₂: Lattice Cu⁺ accelerates carrier migration to the surface of metal copper for photocatalytic CO₂ reduction, Appl. Catal. B 264 (2020), 118515, <https://doi.org/10.1016/j.apcatb.2019.118515>.
- [12] C. Yang, Q. Tan, Q. Li, J. Zhou, J. Fan, B. Li, J. Sun, K. Lv, 2D/2D Ti₃C₂ MXene/g-C₃N₄ nanosheets heterojunction for high efficient CO₂ reduction photocatalyst: dual effects of urea, Appl. Catal. B 268 (2020), 118738, <https://doi.org/10.1016/j.apcatb.2020.118738>.
- [13] J. Xiong, X.B. Li, J.T. Huang, X.M. Gao, Z. Chen, J.Y. Liu, H. Li, B.B. Kang, W. Q. Yao, Y.F. Zhu, CN/rGO@BPQDs high-low junctions with stretching spatial charge separation ability for photocatalytic degradation and H₂O₂ production, Appl. Catal. B 266 (2020), 118602, <https://doi.org/10.1016/j.apcatb.2020.118602>.
- [14] C. Wang, H. Huang, B. Weng, D. Verhaeghe, M. Keshavarz, H. Jin, B. Liu, H. Xie, Y. Ding, Y. Gao, H. Yuan, J.A. Steele, J. Hofkens, M.B.J. Roeffaers, Planar heterojunction boosts solar-driven photocatalytic performance and stability of halide perovskite solar photocatalyst cell, Appl. Catal. B 301 (2022), 120760, <https://doi.org/10.1016/j.apcatb.2021.120760>.
- [15] B. Qiu, P. Huang, C. Lian, Y. Ma, M. Xing, H. Liu, J. Zhang, Realization of all-in-one hydrogen-evolving photocatalysts via selective atomic substitution, Appl. Catal. B 298 (2021), 120518, <https://doi.org/10.1016/j.apcatb.2021.120518>.
- [16] L. Xu, F. Zhang, X. Song, Z. Yin, Y. Bu, Construction of reduced graphene oxide-supported Ag-Cu₂O composites with hierarchical structures for enhanced photocatalytic activities and recyclability, J. Mater. Chem. A 3 (2015) 5923–5933, <https://doi.org/10.1039/C4TA06772J>.
- [17] P.D. Tran, S.K. Batabyal, S.S. Pramana, J. Barber, L.H. Wong, S.C.J. Loo, A cuprous oxide-reduced graphene oxide (Cu₂O-rGO) composite photocatalyst for hydrogen generation: employing rGO as an electron acceptor to enhance the photocatalytic activity and stability of Cu₂O, Nanoscale 4 (2012) 3875–3878, <https://doi.org/10.1039/C2NR30881A>.
- [18] P. Wang, S. Zhan, Y. Xia, S. Ma, Q. Zhou, Y. Li, The fundamental role and mechanism of reduced graphene oxide in rGO/Pt-TiO₂ nanocomposite for high-performance photocatalytic water splitting, Appl. Catal. B 207 (2017) 335–346, <https://doi.org/10.1016/j.apcatb.2017.02.031>.
- [19] W.-K. Jo, S. Kumar, S. Eslava, S. Tonda, Construction of Bi₂WO₆/RGO/g-C₃N₄ 2D/2D hybrid Z-scheme heterojunctions with large interfacial contact area for efficient charge separation and high-performance photoreduction of CO₂ and H₂O into solar fuels, Appl. Catal. B 239 (2018) 586–598, <https://doi.org/10.1016/j.apcatb.2018.08.056>.
- [20] Q. Quan, S.J. Xie, B. Weng, Y. Wang, Y.J. Xu, Revealing the double-edged sword role of graphene on boosted charge transfer versus active site control in TiO₂ nanotube arrays@RGO/MoS₂ heterostructure, Small 14 (2018), 1704531, <https://doi.org/10.1002/smll.201704531>.
- [21] Z.-w Wang, Y.-z Shi, C. Liu, Y.-y Kang, L. Wu, Cu⁺-Ti³⁺ interface interaction mediated CO₂ coordination model for controlling the selectivity of photocatalytic reduction CO₂, Appl. Catal. B 301 (2022), 120803, <https://doi.org/10.1016/j.apcatb.2021.120803>.

- [22] W. Ma, S. Xie, X.-G. Zhang, F. Sun, J. Kang, Z. Jiang, Q. Zhang, D.-Y. Wu, Y. Wang, Promoting electrocatalytic CO₂ reduction to formate via sulfur-boosting water activation on indium surfaces, *Nat. Commun.* 10 (2019) 892, <https://doi.org/10.1038/s41467-019-08805-x>.
- [23] W. Zhang, G. Li, H. Liu, J. Chen, S. Ma, M. Wen, J. Kong, T. An, Photocatalytic degradation mechanism of gaseous styrene over Au/TiO₂@CNTs: relevance of superficial state with deactivation mechanism, *Appl. Catal. B* 272 (2020), 118969, <https://doi.org/10.1016/j.apcatb.2020.118969>.
- [24] T. Soltani, X. Zhu, A. Yamamoto, S.P. Singh, E. Fudo, A. Tanaka, H. Kominami, H. Yoshida, Effect of transition metal oxide cocatalyst on the photocatalytic activity of Ag loaded CaTiO₃ for CO₂ reduction with water and water splitting, *Appl. Catal. B* 286 (2021), 119899, <https://doi.org/10.1016/j.apcatb.2021.119899>.
- [25] Y. Wei, J. Liu, Z. Zhao, Y. Chen, C. Xu, A. Duan, G. Jiang, H. He, Highly active catalysts of gold nanoparticles supported on three-dimensionally ordered macroporous LaFeO₃ for soot oxidation, *Angew. Chem. Int. Ed.* 50 (2011) 2326–2329, <https://doi.org/10.1002/anie.201006014>.
- [26] D. Zhang, H. Zhang, L. Guo, K. Zheng, X. Han, Z. Zhang, Delicate control of crystallographic facet-oriented Cu₂O nanocrystals and the correlated adsorption ability, *J. Mater. Chem.* 19 (2009) 5220–5225, <https://doi.org/10.1039/B816349A>.
- [27] Z. Liu, X. Duan, X. Zhou, G. Qian, J. Zhou, W. Yuan, Controlling and formation mechanism of oxygen-containing groups on graphite oxide, *Ind. Eng. Chem. Res.* 53 (2014) 253–258, <https://doi.org/10.1021/ie403088t>.
- [28] S. Deng, V. Tjoa, H.M. Fan, H.R. Tan, D.C. Sayle, M. Olivo, S. Mhaisalkar, J. Wei, C. H. Sow, Reduced graphene oxide conjugated Cu₂O nanowire mesocrystals for high-performance NO₂ gas sensor, *J. Am. Chem. Soc.* 134 (2012) 4905–4917, <https://doi.org/10.1021/ja211683m>.
- [29] L. Liu, X. Gu, C. Sun, H. Li, Y. Deng, F. Gao, L. Dong, In situ loading of ultra-small Cu₂O particles on TiO₂ nanosheets to enhance the visible-light photoactivity, *Nanoscale* 4 (2012) 6351–6359, <https://doi.org/10.1039/C2NR31859H>.
- [30] P. Zhang, J. Xiong, Y. Wei, Y. Li, Y. Zhang, J. Tang, W. Song, Z. Zhao, J. Liu, Exposed {001} facet of anatase TiO₂ nanocrystals in Ag/TiO₂ catalysts for boosting catalytic soot combustion: The facet-dependent activity, *J. Catal.* 398 (2021) 109–122, <https://doi.org/10.1016/j.jcat.2021.04.015>.
- [31] J. Yu, M. Yang, J. Zhang, Q. Ge, A. Zimina, T. Pruessmann, L. Zheng, J.-D. Grunwaldt, J. Sun, Stabilizing Cu⁺ in Cu/SiO₂ Catalysts with a Shattuckite-Like Structure Boosts CO₂ Hydrogenation into Methanol, *ACS Catal.* 10 (2020) 14694–14706, <https://doi.org/10.1021/acscatal.0c04371>.
- [32] Y. Liu, Z. Zhang, Y. Fang, B. Liu, J. Huang, F. Miao, Y. Bao, B. Dong, IR-Driven strong plasmonic-coupling on Ag nanorices/W₁₈O₄₉ nanowires heterostructures for photo/thermal synergistic enhancement of H₂ evolution from ammonia borane, *Appl. Catal. B* 252 (2019) 164–173, <https://doi.org/10.1016/j.apcatb.2019.04.035>.
- [33] K. Ding, A. Gulec, A.M. Johnson, N.M. Schweitzer, Identification of active sites in CO oxidation and water-gas shift over supported Pt catalysts, *Science* 350 (2015) 6257, <https://doi.org/10.1126/science.aac6368>.
- [34] C.Y. Toe, Z. Zheng, H. Wu, J. Scott, R. Amal, Y.H. Ng, Photocorrosion of cuprous oxide in hydrogen production: rationalising self-oxidation or self-reduction, *Angew. Chem. Int. Ed.* 57 (2018) 13613–13617, <https://doi.org/10.1002/anie.201807647>.
- [35] Y. Li, H. Zhang, P. Liu, D. Wang, Y. Li, H. Zhao, Cross-linked g-C₃N₄/rGO nanocomposites with tunable band structure and enhanced visible light photocatalytic activity, *Small* 9 (2013) 3336–3344, <https://doi.org/10.1002/smll.201203135>.
- [36] Z.F. Jiang, H.L. Sun, T.Q. Wang, B. Wang, W. Wei, H.M. Li, S.Q. Yuan, T.C. An, H. J. Zhao, J.G. Yu, P.K. Wong, Nature-based catalyst for visible-light-driven photocatalytic CO₂ reduction, *Energ. Environ. Sci.* 11 (2018) 2382–2389, <https://doi.org/10.1039/c8ee01781f>.
- [37] H. Mou, C. Song, Y. Zhou, B. Zhang, D. Wang, Design and synthesis of porous Ag/ZnO nanosheets assemblies as super photocatalysts for enhanced visible-light degradation of 4-nitrophenol and hydrogen evolution, *Appl. Catal. B* 221 (2018) 565–573, <https://doi.org/10.1016/j.apcatb.2017.09.061>.
- [38] P. Chen, B. Lei, Xa Dong, H. Wang, J. Sheng, W. Cui, J. Li, Y. Sun, Z. Wang, F. Dong, Rare-earth single-atom La–N charge-transfer bridge on carbon nitride for highly efficient and selective photocatalytic CO₂ reduction, *ACS Nano* 14 (2020) 15841–15852, <https://doi.org/10.1021/acsnano.0c07083>.
- [39] H. Kisch, Semiconductor photocatalysis—mechanistic and synthetic aspects, *Angew. Chem. Int. Ed.* 52 (2013) 812–847, <https://doi.org/10.1002/anie.201201200>.
- [40] X. Chen, L. Liu, P.Y. Yu, S.S. Mao, Increasing solar absorption for photocatalysis with black hydrogenated titanium dioxide nanocrystals, *Science* 331 (2011) 746–750, <https://doi.org/10.1126/science.1200448>.
- [41] F. Zhang, Y.-H. Li, M.-Y. Qi, Z.-R. Tang, Y.-J. Xu, Boosting the activity and stability of Ag-Cu₂O/ZnO nanorods for photocatalytic CO₂ reduction, *Appl. Catal. B* 268 (2020), 118380, <https://doi.org/10.1016/j.apcatb.2019.118380>.
- [42] M.M. Li, D.G. Li, Z.R. Zhou, P.F. Wang, X.Y. Mi, Y.G. Xia, H.T. Wang, S.H. Zhan, Y. Li, L.M. Li, Plasmonic Ag as electron-transfer mediators in Bi₂MoO₆/Ag-AgCl for efficient photocatalytic inactivation of bacteria, *Chem. Eng. J.* 382 (2020), 122762, <https://doi.org/10.1016/j.cej.2019.122762>.
- [43] S.H. Xie, Y.X. Liu, J.G. Deng, J. Yang, X.T. Zhao, Z. Han, K.F. Zhang, Y. Lu, F.D. Liu, H.X. Dai, Carbon monoxide oxidation over rGO-mediated gold/cobalt oxide catalysts with strong metal-support interaction, *ACS Appl. Mater. Interfaces* 12 (2020) 31467–31476, <https://doi.org/10.1021/acsami.0c07754>.
- [44] H. Zhang, Q. Hong, J. Li, F. Wang, X. Huang, et al., Isolated square-planar copper center in boron imidazolate nanocages for photocatalytic reduction of CO₂ to CO, *Angew. Chem. Int. Ed.* 58 (2019) 11752–11756, <https://doi.org/10.1002/ange.201905869>.
- [45] S. Gong, G. Zhu, R. Wang, F. Rao, X. Shi, J. Gao, Y. Huang, C. He, M. Hojamberdiev, Synergistically boosting highly selective CO₂-to-CO photoreduction over BiOCl nanosheets via in-situ formation of surface defects and non-precious metal nanoparticles, *Appl. Catal. B* 297 (2021), 120413, <https://doi.org/10.1016/j.apcatb.2021.120413>.
- [46] B. Wang, J. Di, L. Lu, S.C. Yan, G.P. Liu, Y.Z. Ye, H.T. Li, W.S. Zhu, H.M. Li, J.X. Xia, Sacrificing ionic liquid-assisted anchoring of carbonized polymer dots on perovskite-like PbBiO₂Br for robust CO₂ photoreduction, *Appl. Catal. B* 254 (2019) 551–559, <https://doi.org/10.1016/j.apcatb.2019.04.068>.
- [47] Q. Geng, H. Xie, Y. He, Y. Sun, X. Hou, W. Zhiming, F. Dong, Atomic interfacial structure and charge transfer mechanism on in-situ formed BiOI/Bi₂O₂SO₄ p–n heterojunctions with highly promoted photocatalysis, *Appl. Catal. B* 297 (2021), 120492, <https://doi.org/10.1016/j.apcatb.2021.120492>.
- [48] X. Li, Y. Sun, J. Xu, Y. Shao, J. Wu, X. Xu, Y. Pan, H. Ju, J. Zhu, Y. Xie, Selective visible-light-driven photocatalytic CO₂ reduction to CH₄ mediated by atomically thin CuIn₂S₃ layers, *Nat. Energy* 4 (2019) 690–699, <https://doi.org/10.1038/s41560-019-0431-1>.
- [49] J. Wang, T. Bo, B. Shao, Y. Zhang, L. Jia, X. Tan, W. Zhou, T. Yu, Effect of S vacancy in Cu₃SnS₄ on high selectivity and activity of photocatalytic CO₂ reduction, *Appl. Catal. B* 297 (2021), 120498, <https://doi.org/10.1016/j.apcatb.2021.120498>.
- [50] J. Li, H. Huang, W. Xue, K. Sun, X. Song, et al., Self-adaptive dual-metal-site pairs in metal-organic frameworks for selective CO₂ photoreduction to CH₄, *Nat. Catal.* 4 (2021) 719–729, <https://doi.org/10.1038/s41929-021-00665-3>.
- [51] X. Qiu, H. Zhu, J. Huang, P. Liao, X. Chen, Highly selective CO₂ electroreduction to C₂H₄ using a metal-organic framework with dual active sites, *J. Am. Chem. Soc.* 143 (2021) 7242–7246, <https://doi.org/10.1021/jacs.1c01466>.
- [52] X. Liu, J. Xiao, H. Peng, X. Hong, K. Chan, J.K. Nørskov, Understanding trends in electrochemical carbon dioxide reduction rates, *Nat. Commun.* 8 (2017) 15438, <https://doi.org/10.1038/ncomms15438>.